The Distribution of Mg-Spinel across the Moon and Constraints on Crustal Origin

Carle M. Pieters[1]
Kerri Donaldson Hanna[1]
Leah Cheek[1]
Deepak Dhingra[1]
Tabb Prissel[1]
Colin Jackson[1]
Daniel Moriarty[1]
Stephen Parman[1]
Lawrence A. Taylor[2]

[1]Department of Geological Sciences, Brown University, Providence, RI 02912 USA
[2]Planetary Geosciences Institute; University of Tennessee, Knoxville, TN 37996 USA

Submitted to American Mineralogist [special issue on Lunar Highland Crust (and Spinels?)]
DATE: October 2013 REVISED: February 2014

Abstract

A robust assessment is made of the distribution and (spatially resolved) geologic context for the newly identified rock type on the Moon, a Mg-spinel-bearing anorthosite (Pink-Spinel Anorthosite, PSA). Essential criteria for confirmed detection of Mg-spinel using spectroscopic techniques are presented and these criteria are applied to recent data from the Moon Mineralogy Mapper. Altogether, 23 regions containing confirmed exposures of the new Mg-spinel rock type are identified. All exposures are in highly feldspathic terrain and are small – a few hundred meters - but distinct and verifiable, most resulting from multiple measurements. Each confirmed detection is classified according to geologic context along with other lithologies identified in the same locale. Confirmed locations include areas along the inner rings of four mascon basins, knobs within central peaks of a few craters, and dispersed exposures within the terraced walls of several large craters. Unexpected detections of Mg-spinel are also found at a few areas of hypothesized non-mare volcanism. The small Mg-spinel exposures are shown to be global in distribution, but generally associated with areas of thin crust. Confirmation of Mg-spinel exposures as part of the inner ring of four mascon basins indicates this PSA rock type is principally of lower crust origin and predates the basin-forming era.

Keywords: spinel, lunar crust, spectroscopy, Moon Mineralogy Mapper

1 Introduction

The suite of orbital spacecraft recently sent to the Moon by Japan, India, China, and the United States included several modern instruments capable of performing a first-order evaluation of lunar mineral composition at high spatial and high spectral resolution (e.g., Ohtake et al., 2013; Pieters et al., 2013a). Among the abundant fundamental scientific findings, one unexpected result was discovery of a new feldspathic rock type with spectral features dominated by (Mg,Al)-spinel exposed at small localized areas on the lunar surface (Pieters et al., 2011). The most common forms of spinel found on the Moon are Fe, Cr, or Ti-rich opaque minerals (e.g., Haggerty, 1978; see also summary in Prissel et al. 2014). Small amounts of transparent Mg,Al-rich spinel ("pink spinel") have been identified in a few lunar samples, but they have always been found to occur in association with relatively abundant olivine or other mafic minerals (e.g., Gross & Treiman, 2011). Throughout the discussion below, we will refer to this form of non-opaque, low (Fe, Cr, Ti) spinel stricto sensu simply as 'Mg-spinel'.

Since this new Mg-spinel-bearing rock type has not been identified among the returned lunar samples, its recognition has sparked extensive observational, experimental, and theoretical analyses to constrain the occurrence and petrologic characteristics of Mg-spinel on the Moon (Gross and Treiman, 2011; Prissel et al. 2012, 2013, 2014; Jackson et al. 2012, 2014). The principal exposures of the new Mg-spinel rock type identified to date and discussed below contain no detectible common mafic minerals (less than ~5% olivine, pyroxene) and are always found in a low-Fe terrain dominated by plagioclase feldspar. This has been interpreted to mean that the new rock type is itself feldspathic, a 'pink spinel anorthosite' or PSA (Taylor and Pieters. 2013). Constraints on the spinel/plagioclase ratio are also under investigation with laboratory and analytical mixing experiments (e.g., Dhingra et al., 2011b; Cheek et al., 2014).

The goals of the integrated analyses presented here are to discuss robust criteria for the identification of this new PSA rock type and to summarize characteristics of the range of observed spinel-bearing lithologies found across the Moon. The association of several key exposures with the inner ring of a few mascon basins implies that the origin of this new rock type is ancient and a widespread component of the lower crust of the Moon.

2 Identification of Mg-Spinel

2.1 Diagnostic Properties

The spectroscopic detection of spinel-rich regions across the Moon requires a) high spectral resolution near-infrared measurements to recognize diagnostic absorption features and b) high spatial resolution and two-dimensional contiguous coverage to detect sub-kilometer exposures. Due to its composition and crystal structure, non-opaque spinel exhibits two strong absorptions that are highly diagnostic and occur near 2000 and 3000 nm, respectively (e.g., Cloutis et al. 2004). These two absorptions are due to electronic transitions of ferrous iron in a tetrahedral environment and the dual bands are believed to be associated with additional crystal field splitting of the energy levels of d-orbital electrons. Such d-orbital electronic transitions of ferrous iron in a tetrahedral environment are typically very strong (Burns, 1993), and only minor amounts of iron are required in the crystal structure. Typical laboratory reflectance spectra of two compositions of spinel, a Mg-spinel and a chromite, are shown in **Figure 1** in comparison with common lunar minerals.

The remote identification of spinel is enabled by its unique spectral properties with respect to those of other minerals found on the lunar surface. The most common mafic mineral found in the lunar crust, pyroxene, always exhibits two prominent ferrous iron absorptions near 1000 and 2000 nm, the specific wavelengths of which depend on the composition (and ultimately structure) of the pyroxene present (e.g., Burns 1993; Klima et al., 2007, 2011). Olivine is dominated by a multi-component ferrous absorption that is centered slightly longer than 1000 nm. Pure olivine exhibits no features between 1600 and 2600 nm. Even crystalline plagioclase with trace amounts of ferrous iron exhibits a diagnostic absorption near 1250 nm. Mg-spinel, on the other hand, is dominated by the two characteristic strong absorptions at longer wavelengths (1500-3000 nm) with no significant absorptions at shorter wavelengths. In contrast, the more Fe- and Cr-rich spinels (e.g., chromite) exhibit a range of absorptions across 300-1000 nm, causing them to be darker and respond as opaque.

Using data from the Moon Mineralogy Mapper (M^3) near-infrared imaging spectrometer (Pieters et al., 2009; Green et al., 2011), the initial detections of Mg-spinel (Pieters et al., 2011) relied on several spectroscopic criteria. These are illustrated in **Figure 2**: 1) presence of the two absorption bands near 2000 and 3000 nm (large arrows) that are diagnostic of spinel; 2) absence of any significant absorption band(s) near 1000 nm which would otherwise indicate the presence of pyroxene; and 3) an implicit third requirement being a lack of abundant dispersed opaque phases that would prevent radiation from interacting with semi-transparent minerals present and thus prevent diagnostic absorptions from being observed. An obvious fourth requirement is consistency: 4) if an area is observed more than once, independent data must meet the same criteria. This repeatability criterion is necessary given the complex calibration challenges encountered by M^3 (e.g., Boardman et al., 2011; Lundeen et al., 2011). Although M^3 data cannot fully resolve the second spinel absorption near 3000 nm, the first criterion is met by detection of the band near 2000 nm along with an inflection peak between the two absorptions (Fig. 2, small arrow). Since pyroxenes are ubiquitous across the Moon, the second criterion (lack of 1000 nm feature) is essential in order to eliminate this common mineral as the source of any feature observed near 2000 nm. However, the composition of spinel that can be confidently detected with this criterion may also be limited to be Mg-rich (e.g. Cloutis et al., 2004; Jackson et al., 2014). This approach to spinel detection necessarily focuses on featureless or feldspathic terrain and cannot easily recognize Mg-spinel if it occurs within areas that contain abundant mafic minerals.

Unfortunately, not all 'features' detected in near-infrared spectra are due to mineralogy of the surface. Near-infrared radiation from the Moon near 3000 nm commonly contains a natural component of thermally-emitted radiation in addition to the reflected solar radiation. Isolating only the reflected radiation that has interacted with surface components is needed in order to evaluate absorption bands in reflectance spectra similar to those of Figure 1. The M^3 data available through the NASA Planetary Data System (PDS) have had a first order thermal component estimated and removed during calibration (Clark et al., 2011). The thermal-removal approximation used for standard M^3 products, nevertheless, often leaves a small component of thermal radiation that results in a higher signal towards longer wavelengths. Such a minor residual-thermal component can mimic a weak band near 2000 nm and can easily be misinterpreted as suggesting the presence of spinel. As an important guideline to spinel-hunters, we note that for most spectra of Mg-spinel-rich areas on the Moon, the inflection of the continuum at the beginning of the first spinel band occurs at wavelengths shorter than 1500 nm. During data acquisition, M^3 also encountered several environmental challenges (Boardman et al., 2011) that resulted in a variety of data artifacts that could not be removed during calibration (Lundeen et al., 2011). Many occur at wavelengths below 1000 nm and may obscure the character of short-wavelength features, if present. When available, multi-temporal M^3 observations taken under different viewing geometries can frequently resolve ambiguities associated with feature identification.

The strength of an absorption band for a soil or mixture of minerals is dependent on the relative abundance of the absorbing species, independent of the presence or absence of measurement artifacts in spectra. In a mixture, the relative strengths of features from different minerals combine non-linearly, and darker, more absorbing components dominate a composite spectrum. For example, in a pyroxene-plagioclase mixture, pyroxene features dominate the spectrum even when pyroxene is only 5-15 % of the mixture (e.g. Cheek et al., 2014). Similarly, the cumulative effects of strongly absorbing space weathering components dramatically affect the strength of absorption bands in a highly non-linear manner. As soils accumulate weathering products with exposure to the space environment on the lunar surface, absorption bands weaken, surface brightness becomes more subdued, and a generally 'red-sloped' continuum is developed (Pieters et al., 2000; Hapke 2001). For example, the Apollo 16 soil in Figure 1, derived principally from rocks and breccias at the site, exhibits the classic characteristics of extensive lunar space weathering products.

2.2 Mapping of Mg-Spinel from Orbit

The diagnostic spectral properties of spinel are well founded in mineral physics, and such characteristics should make them readily detectible with high-quality imaging-spectrometer data. However, due to possible residual thermal signal and/or measurement-condition artifacts, no single parameter or automated algorithm can be used with M^3 data to reliably identify and map spinel with certainty. We have taken a combination of approaches to assess the general global distribution as well as the character and context of local exposures. Several spectral parameters sensitive to known properties of lunar materials (e.g., Figures 1, 2) have been developed and we used them for a first-order evaluation of possible exposures of plagioclase and/or spinel. We examined: a) M^3 global mosaics at low spatial resolution (~1 km) and b) catalogued craters with central peaks at full resolution (see discussion in Donaldson Hanna et al., 2014). We also examined possible detections mentioned in the literature if sufficient information was provided for location (e.g., Lal et al., 2011, 2012, Kaur et al., 2012, 2013a, b, Srivastava and Gupta, 2012, Bhattacharya et al., 2012, 2013, Yamamoto et al., 2013, Sun et al, 2013; Kaur and Chauhan, 2014; Chauhan et al., 2014). Unfortunately, a large number did not meet the criteria described in section 2.1 and were not pursued further.

Each potential candidate area was then evaluated in more detail with a closer evaluation of criteria described in Section 2.1. Since spurious 'features' mentioned above can easily lead to misidentification, we searched for independent measurements (multiple M^3 observations taken at different times) of the same area, preferably with significantly different measurement conditions (e.g., illumination, phase angle, surface temperature, detector temperature), to evaluate the criteria and to confirm (or not) the detection of Mg-spinel. In the discussion below we use the distribution of materials in Theophilus crater to illustrate results and tests applied for different candidate areas. The resulting global distribution of Mg-spinel and implications for the lunar crust are discussed in subsequent sections.

The central part of Theophilus crater was observed twice by M^3, approximately six months apart during two different optical periods (OP). Both were morning observations, acquired when the detector was cold (see Boardman et al., 2011). Example M^3 image-cube data for the low-altitude orbit OP1b measurements (at 100 km altitude) centered on the central peaks are shown in **Figure 3**. The base image is reflectance at 1489 nm, with photometric corrections applied to a sphere (found in PDS *_SUP.IMG #1), thus retaining information about illumination geometry of the scene. These data, and most M^3 images shown later, have not been re-configured to lunar map projections, since spatial resolution is degraded by such resampling. Similar independent data for Theophilus obtained during OP2c3 are presented for comparison as Figure S3 in supplementary information.

The central peaks of Theophilus are considerably brighter than surroundings, consistent with a low-mafic, highly feldspathic character originally suggested from telescopic spectra (e.g., Pieters, 1986). At the higher spatial resolution of M^3 (140 m/pixel), the peaks are seen to be comprised of two principal lithologies, both highly feldspathic with very low mafics but one of which contains relatively abundant Mg-spinel (Dhingra et al., 2011b,c). Representative spectra extracted from this image cube are shown in **Figure 4**a; all but one of which are from the central peaks. The data obtained later during OP2c3 were from a higher-altitude orbit (200 km) and thus lower spatial resolution. Nevertheless, five areas that can be co-located (Figure 4b) exhibit spectra with the same fundamental properties within measurement noise and illumination differences (brightness) resulting from local topography.

For these and all subsequent figures with M^3 spectra, we do not smooth the data in wavelength, thus allowing any artifacts to be visible. In order to maintain the highest spatial resolution, most spinel spectra are for individual pixels, whereas background soil areas used for comparison are for 3x3 or 5x5 pixel averages. We indicate the specific optical period (OP) during which the spectra were acquired, as well as an indication of the detector temperature (warm or cold) which links to the calibrations applied (Boardman et al., 2011; Lundeen et al., 2011).

The spectra of Figure 4 have been classified according to the optically dominant mineral of their lithology that can be derived from prominent diagnostic features – i.e., Mg-spinel-bearing (green), low-mafic plagioclase-rich (blue), and pyroxene-bearing (red). Although all these spectra also necessarily contain some level of subdued space weathering alteration, we use the regular features seen in the M^3 spectra to define several simple spectral parameters that can provide a first-order regional assessment, while being directly linked to well-known diagnostic absorptions of lunar materials (Figure 1). The formulations of these parameters are summarized in **Table 1**, and key elements are illustrated graphically in **Figure 5**. For the plagioclase and short-wavelength pyroxene bands approximate band strength is calculated using two wavelengths on symmetric sides of the band to estimate a continuum and a value near the center to estimate the strength of the absorption. For spinel, however, since only the short wavelengths of the composite absorption bands are measured, we use a band ratio to approximate variations in band strength. A good approximation of a formal band-depth value (e.g., Clark et al., 2003) can be derived from the parameters in Table 1 by inverting the parameter (1/x) and subtracting from unity. Values for these parameters are calculated for each pixel in the M^3 scene producing a derived image for each parameter.

We stress that such parameter images are designed primarily to provide a guideline to evaluate local lithology variations. They are not a quantitative tool, but capture regional variations reasonably well and may highlight unusual areas. They are best used to identify the type and spatial extent of prominent lithologies present in a region. Each of the parameter images calculated for the M^3 image cube of Figure 3 has been contrast stretched to highlight only areas with the strongest absorption. These have then been made into a color-composite with the color assignments indicated in Table 1 to reflect the following absorption strength approximations: Red=pyroxene, Green=spinel, and Blue=crystalline plagioclase. This color-composite is then merged (~50%) with the 1489 nm brightness image in **Figure 3b**.

Although Theophilus may currently provide the best Mg-spinel exposure on the Moon, it is also a good example of many of the properties observed elsewhere. The Mg-spinel-bearing areas occur as small knobs (on the floor) or discrete outcrops (in the central peaks) that are only a few hundred meters in extent. Except for where there is clearly down-slope movement and mixing, mineralogical boundaries are sharp. Plagioclase is the dominant neighboring lithology, and at Theophilus it often occurs in crystalline form (with its distinct 1250 nm ferrous band). It should be noted that the plagioclase absorption at Theophilus is typically very weak (the blue stretch in Figure 3b also picks up random 'striping' of the data).

Theophilus also exhibits several properties that are unique to the local geology. There is a hint of olivine present in only one of the peaks (area #6). This feature would normally be discounted as random variations if it were not repeatable during the later independent measurement. Note that with these limited three parameters, olivine-rich materials are often highlighted by the plagioclase parameter and appear "blue" in the color-composite. The small knobs containing Mg-spinel to the SW of the peaks are real and suggest that area has some affiliation with the peaks. The NW-SE valley between peaks contains what might be mixtures of crystalline plagioclase and Mg-spinel, although whether it is a physical mixture of two components or a separate lithology has yet to be explored with mixing constraints (e.g. Cheek et al. 2014). Only one small area of a few pixels in extent in the middle of the southern peak contains any pyroxene. Although the southern rim is devoid of mafic minerals, the north rim of the crater contains relatively abundant pyroxene content. This might be associated with the maria further to the north, but is without a direct link to any specific basaltic unit.

3 Global Distribution and Geologic Context

The procedures used to evaluate the Theophilus region were used for areas identified as possibly containing Mg-spinel. These include areas identified by our group, as well as those from the literature referenced above that were accessible in M^3 data and for which the criteria described in Section 2.1 could be examined. Many areas in the literature were not evaluated further because published information violated the criteria of Section 2.1, usually by the presence of a feature near 1000 nm (likely due to the presence of pyroxene) or by a weak 2000 feature without inflection for the second spinel band (likely residual thermal contribution or artifact). The strongest candidates were assigned a number in approximate order of their detection. Under further scrutiny, several additional areas were excluded because they provided conflicting results when evaluated with independent measurements. The areas examined that met the criteria of section 2.1 are summarized in **Table 2** along with the M^3 files used in the evaluation. For some areas spanning a large spatial extent, two contiguous files are included to provide an example of longitudinal coverage. Most of the confirmed Mg-spinel-bearing PSA locations listed in Table 2 have independent data showing consistent results. For areas that have no independent data available for analysis, we provide a tentative confirmation and classification only if the exposures appear to meet all other criteria.

The distribution of confirmed exposures of the new Mg-spinel bearing PSA rock type is shown with oversized symbols in **Figure 6**. As at Theophilus, the exposures themselves are only a few hundred meters in size. In all cases, the host lithology that dominates the region around the Mg-spinel exposure is highly feldspathic, usually with no detectible absorption features.

Small exposures of feldspathic lithology containing low-Ca pyroxene often occur in other neighboring areas (but not always), and in a few instances, olivine may be present nearby. These associations are summarized in Table 2 and discussed further with individual spectra below.

For discussion purposes, we have classified the Mg-spinel occurrences for each of the confirmed areas into one of five groups, according to their geologic context: **[B]** A few areas occur in association with mascon basins along what would be the inner ring of the basin. These areas are central in identifying the source region of Mg-spinel and are discussed in Section 4. The remaining exposures occur in diverse terrain and are discussed separately in Section 5. **[K]** Several occurrences are found as small knobs associated with the central peaks of large craters. Typically they are found near the periphery of the peaks and impact melt is often nearby. **[D]** A significant number occur as (apparently) random blocks dispersed in the walls or deposits of large impact craters. Some of these craters contain central peaks, usually without spinel. **[S]** A few Mg-spinel exposures occur in special highland areas. These include two floor fractured craters and a few areas of possible highland volcanism. **[P]** For completeness, we include the single regional pyroclastic deposit that is now known to contain abundant spinel, although the composition of the spinel appears to be different (Sunshine et al., 2010; Yamamoto et al., 2013). Lower-case symbols in Figure 6 indicate tentative confirmation.

4 Basin Exposures of Mg-Spinel

Four of the key and unambiguous detections of Mg-spinel (1-Moscoviense, 2-Theophilus, 14-Thomson/Ingenii, 18-Montes Teneriffe) are located in regions with very-thin crust associated with mascon basins. The geologic context of these areas (Fig. 6) provides important constraints on the source area of Mg-spinel in the lunar crust. For both Moscoviense and Montes Teneriffe, the Mg-spinel exposures occur directly on the flanks of the inner ring of the basin, Moscoviense and Imbrium basins, respectively. At Theophilus and Thomson, Mg-spinel was exposed by these craters that impacted into the inner rings of Nectaris and South Pole-Aitken (SPA) basins, respectively.

It should be noted that compositional analyses of the Orientale basin, the youngest and perhaps the best-exposed basin on the Moon, support the model of the inner ring as a distinct uplifted component of crustal stratigraphy (e.g., Spudis 1993; Head 2010). In the case of Orientale, the inner ring is observed to be a massive zone of 'pure' anorthosite that spans across the entire basin (e.g. Cheek et al. 2013) and most likely represents the fundamental product of magma-ocean differentiation (e.g., Hawke et al., 2003a; Ohtake et al., 2009). Identifying locations where the composition of the inner ring of basins is exposed provides access to crustal composition and stratigraphy, and may be the closest cousin to bedrock available to lunar scientists.

4.1 Moscoviense and Imbrium Basins

The character and physical properties of the Moscoviense exposures are discussed in detail in Pieters et al. (2011) and will not be repeated here. The basin materials are highly feldspathic in overall composition. Mg-spinel-bearing PSA is one of three types of locally unusual lithologies exposed in distinct and widely separated areas along the inner ring of the basin. These unusual areas were termed "OOS" for the dominant mineral present at each location – i.e., Olivine, Orthopyroxene, Spinel. None of these areas are disturbed by later activity (craters), and all exhibit well-developed soil comparable to their surroundings. Example M^3 spectra are shown in **Figure 7** for Moscoviense areas that exhibit these three lithologies as measured during two independent optical periods. Rock-type color-composite images for Moscoviense prepared similar to Figure 3 re-emphasize the spatial relations between the different rock types discussed in Pieters et al. (2011) and is provided as Figure S7 in supplemental data.

An overview of the context for Montes Teneriffe in northern Imbrium is shown in **Figure 8**. This ridge is believed to be one of the few remnants of the inner ring of the Imbrium basin (de Hon, 1979; Spudis, 1993) that has not been covered by mare basalt. Shown in **Figure 9** are M^3 reflectance images and rock-type color-composites across the Montes Teneriffe region similar to Figure 3. Representative spectra for the area are shown in **Figure 10**. A comparison of color-composite images and spectra from three independent optical periods are shown in Figures S9 and S10. Again, the ridge itself is highly feldspathic with no significant Mg- or Fe-bearing minerals (i.e., <5%), except for two distinct exposures of Mg-spinel. Spectra of the mountains forming Montes Teneriffe are largely featureless, although minor low-Ca pyroxene or olivine may occur in a few locations, but these are not confirmed. The basalts filling Imbrium exhibit the typical spectral character dominated by high-Ca pyroxene. Minor amounts of Mg-spinel have recently been detected (Kaur and Chauhan, 2014) and confirmed (27-Sinus Iridum) along the southwest rim of Sinus Iridum and are thus also related to the Imbrium Basin.

Estimates of crustal thickness from recent lunar geophysical data (Ishihara et al., 2009; Wieczorek et al., 2012) show that both the Moscoviense and Montes Teneriffe sites are located in areas of exceptionally thin crust, on the edge of a large mascon associated with the Moscoviense and Imbrium basins (Figure 6). These basins have a rim diameter 420 km and 1160 km respectively. Stratigraphic relations indicate that these feldspathic massifs are a result of the basin-forming impact itself and predate the basaltic lavas that filled the basin. Neither the Moscoviense nor Montes Teneriffe sites show any evidence of being affected by the later emplacement of mafic-rich basalts.

4.2 Nectaris and South Pole-Aitken Basins

The Theophilus and Thomson Mg-spinel sites are situated in a similar geologic context associated with an inner ring of a major basin. However, the basins at both sites, Nectaris and SPA respectively, are older than Moscoviense and Imbrium, and exposure of Mg-spinel at Theophilus and Thomson has occurred through additional impact events onto what is believed to represent the inner ring of the basins. Theophilus crater is 100 km in diameter and Thomson crater is 117 km; the Nectaris basin is 860 km in diameter, whereas SPA is enormous at ~2500 km. An overview of the two sites is shown in **Figure 11**.

The character of Mg-spinel-bearing PSA and associated lithologies exposed across the central peaks of Theophilus was presented in Section 2.2 above. Diagnostic spectral features identified in data from both optical periods (Figure 4) are quite consistent. The overview of OP1b data presented in Figure 3 and the independent data from OP2c3 provided as Figure S1 show the same patterns of Mg-spinel in geologic context.

Recent data from the GRAIL spacecraft (Wieczorek et al., 2012) indicate that the site of the Theophilus impact is actually where two contiguous mascons appear to intersect (Figure 6). Although Theophilus contains the best exposure of Mg-spinel lithology found on the Moon to date, a much older and more subdued crater (Cyrillus) to the west of similar size (see. Figure 11) exhibits no trace of spinel. The unusual geophysical setting and dominance of plagioclase and Mg-spinel in the central peaks of Theophilus suggests this material represents a re-excavation of relatively pristine bedrock originally exposed in the inner ring of Nectaris basin.

On the other hand, the exposures of Mg-spinel at Thomson crater on the farside, although individually small, are currently the most extensive, with spinel observed across both the northern and southern walls of the crater. Shown in **Figure 12** are M^3 data from OP2c2, illustrating several northern and southern exposures in context. An independent mosaic of the entire Thomson crater, using OP2c1 data, is provided as Figure S12 in supplemental information, although spatial resolution is degraded by the re-sampling and projection required for mosaic preparation.

Example Thomson spectra from OP2c1 and OP2c2 for the same areas are shown in **Figure 13**. Mg-spinel-bearing exposures (#1 and 3) are widely separated across a feldspathic (low mafic) terrain. The most common mafic mineral in the non-mare area is low-Ca pyroxene (e.g., #2 and yellow-toned areas in Figure 12). Small craters in the Thomson ejecta to the north expose local areas with more abundant low-Ca pyroxene. The interior of the small 7 km crater along the NW rim exhibits diverse lithologies: pyroxene occurs in the north wall and both crystalline plagioclase and minor olivine (#5) in the south wall. In contrast, the mare basalts that filled Thomson (#4) exhibit characteristic high-Ca pyroxene as noted by the longer wavelength of both pyroxene absorptions. Additional Thomson spectra can be found in Figure S13.

As can be seen from the superposition relation of features in Figure 11, Thomson occurs within the larger Ingenii basin, which itself occurs along the ring of SPA. In recent GRAIL data (Figure 6), Ingenii is a small mascon basin (Wieczorek et al., 2012). Ingenii also contains prominent “swirls”, enigmatic wispy albedo features of unknown origin usually associated with magnetic anomalies (e.g. Blewett et al. 2011, Kramer et al., 2011). Basalts of the farside appear to have been emplaced after the late heavy bombardment, over a period similar to those of the nearside, peaking near 3.5 Ga, but extending perhaps another Ga (e.g., Haruyama et al., 2009). The detailed history of magmatic activity within SPA, however, is not well known.

The material brought to the surface by Thomson pre-existed within Ingenii. Since there is no indication of basaltic material in Thomson rim or ejecta, basaltic magmatism post-date both Ingenii and Thomson in this region. Thus, the heritage of materials now exposed around the rim of Thomson is linked to a special case where products of the SPA impact were excavated by Ingenii and then by Thomson. From the integration of compositional and geophysical information for this region, the sequence of events involve 1) formation of SPA basin, 2) formation of Ingenii basin and mascon, 3) Thomson impact, 4) filling of Ingenii and Thomson with mare basalts, and 5) formation of swirls.

5 Non-Basin Exposures of Spinel

Although none of the sites containing detectible spinel are associated with the area of thick crust on the lunar farside called 'Feldspathic Highland Terrane' by Jolliff et al. (2000), the remaining areas containing Mg-spinel occur in a wide variety of geologic settings (Figure 6). Mg-spinel exposures are typically found as small knobs that occur in the central uplift of large craters or as dispersed exposures in the walls of terraced craters. Examples of each are provided below.

5.1 Mg-Spinel Occurrences

5.1.1 Knobs (K): 8-Albategnius

Most occurrences of Mg-spinel associated with the central peaks of large craters are quite different from that seen at Theophilus. Commonly the Mg-spinel is found in a lesser peak or knob of a central peak complex. Again, the Mg-spinel exposure is usually quite small. The crater Albategnius (#8) on the lunar nearside is a good example. Shown in **Figure 14** is a LROC WAC image of the 129 km diameter crater for overall context. An M^3 color-composite image for the central peak of Albategnius and the western floor is shown in **Figure 15** using the same scheme as that used for Theophilus (Figure 3). At Albategnius, no crystalline plagioclase is exposed, but most of the peak and crater walls are composed of featureless (feldspathic) material. Pyroxene-bearing lithologies are only found in the smooth material of the floor.

Representative individual spectra shown in **Figure 16** illustrate the compositional properties detected across the region. Independent data for the same areas acquired 5 months apart capture the same spectral features and provide validation of their properties, although the data from OP2c have a lower signal-to-noise ratio. To enhance some of the subtle features, we also present the data as relative-reflectance spectra in Figure S16, using the featureless spectrum (#5) as the reference. This procedure is similar to that used in Pieters et al. (2011). If the reference area is indeed 'featureless', relative reflectance can be used to minimize local artifacts and clarify subtle features of the Mg-spinel area (#1). All the criteria for Mg-spinel are met for Albategnius. Based on the wavelength position of the two pyroxene bands for areas #2, 3, and 4, we interpret the pyroxene composition to be low-Ca (LCP), and the smooth-floor material here is thus consistent with noritic rock types rather than of basaltic origin.

A few of the Mg-spinel detections at knobs in or near central-peaks of other craters are found in close association with impact-melt or basaltic infill. These include the small exposures at 3-Copernicus, 4-Tycho, and 13-Joliot. If the interaction of a mafic magma with local anorthositic materials is a principal condition for formation of lunar Mg-spinel (e.g., Prissel et al., 2014), then the spinel observed at these knob locations might be a more recent product of melt-rock interactions on the surface (see discussion in Section 6).

5.1.2 Dispersed (D): 21-Geminus

Several large terraced craters have been found to exhibit small outcrops of Mg-spinel material, scattered in discrete areas in walls, terraces, or ejecta. All spinel exposures occur in a dominant feldspathic context, usually with no neighboring mafic minerals (<5%) although low-Ca pyroxene may be close-by. For most such craters that also have central peaks, no Mg-spinel is seen in their central peaks (7-Werner, 16-Piccolomini, 21-Geminus), with only one exception (9-Walther). Geminus crater on the eastern nearside is a good example of such dispersed exposures of Mg-spinel. A M^3 color-composite image for the northern half of Geminus is shown in **Figure 17.** Small exposures occur along the western wall of Geminus, but most are concentrated in the northern wall. The M^3 spectra for areas indicated with arrows are shown in **Figure 18**. Independent data for the same areas from three optical periods are compared in Figure S18. The spinel absorptions are relatively weak at Geminus and would be strongly suspected to be random artifacts, if only one measurement were available. However, since the features are persistent and consistent in three independent measurements under greatly different measurement conditions, the Geminus Mg-spinel meets the criteria of Section 2.1.

Spectra for a few areas within the wall also contain absorptions indicative of the presence of minor low-Ca pyroxene. The central peaks exhibit clear features suggestive of exposures of low-Ca pyroxene lithologies, as does a fresh crater on the floor (these areas appear yellow in the color-composite of Figure 17). Although Geminus does not exhibit prominent absorptions due to crystalline plagioclase in this area, the plagioclase parameter (blue in color-composite of Figure 17) highlights areas that exhibit weak features indicative of the presence of olivine. The olivine absorption just beyond 1000 nm (purple dotted spectra in Figure 18) is very weak, but highly consistent across independent M^3 measurements. We tentatively interpret this to indicate small zones of troctolite (olivine + plagioclase) occuring along the northern wall as well. Note that the olivine and spinel areas are nearby, but not contiguous with one another.

5.1.3 Special areas (S): 17-Dalton and 25-Hansteen Alpha

There are a few Mg-spinel-bearing areas that merit special discussion. Although they may not fall into a separate category, two areas containing Mg-spinel exposures are associated with floor-fractured craters. These unusual craters are believed to have experienced plutonic magmatic activity (e.g., Schultz, 1976; Jozwiak et al., 2012), and are highlighted separately here, because such igneous events may play a role in the origin of some Mg-spinel (e.g., Prissel et al., 2014). The forms of exposure for the two craters are different. Examples for 17-Dalton crater shown here are similar to the small exposures in knobs of central mounds. At the second floor-fractured crater, 10-Pitatus, exposures occur as small areas along the southern rim of the crater.

Dalton is a 60 km diameter crater on the western limb. Although coverage and resolution were not identical, four independent M^3 measurements were acquired under different conditions. The Mg-spinel-bearing areas are shown in **Figure 19,** using the same color-composite approach as for Figure 3. Similar color-composite images for the other three optical periods are found in Figure S19. Three spectrally distinct, but otherwise unremarkable, areas of Mg-spinel are seen in the central cluster of mounds. No mafic minerals were detected (i.e., <5%), although low-Ca pyroxene is seen in local areas along the western rim (usually exposed by small craters, appearing yellow in Figure 19). Representative spectra are shown in **Figure 20** and comparisons for the same areas for all four optical periods are shown in Figure S20.

If only OP1a data were available, Dalton would not be confirmed as containing Mg-spinel; a weak feature across 1000 nm is observed, suggesting the 2000 nm feature might be due to pyroxene plus residual minor thermal component. However, data from the same areas in other optical periods show that the weak feature near 1000 nm, seen in these OP1a spectra, is largely an artifact and can be disregarded. Most bright material in Dalton exposed at medium-size craters (e.g. Cr-1) is featureless and inferred to be feldspathic, with little mafic content. Note that an example of residual thermal component can also be seen in the spectrum for Cr-1 of OP1b. Due to the low sun geometry for this period, the average area received only small amounts of illumination, but the wall of this crater was oriented so that solar illumination was closer to normal, and it appears more radiation was available for heating that surface.

Mg-spinel has also been discovered recently for two of the areas that have been described as examples of possible non-mare volcanism (Hawke et al., 2003; Jolliff et al., 2011): 25- Hansteen Alpha (Kaur et al., 2013b) and 26-Compton-Belkovich (Bhattacharya et al., 2013). To date, these are the only non-mare volcanism sites that appear to exhibit the presence of Mg-spinel. Two independent M^3 reflectance images and rock-type color-composites, similar to Figure 3 for Hansteen Alpha, are shown in **Figure 21**, and spectra for individual pixels of the same areas from the two different optical periods are compared in **Figure 22**. As seen elsewhere on the Moon, the individual exposures of Mg-spinel in Hansteen Alpha are small and dispersed. Given the much-lower spatial resolution of Earth-based telescopes (several km at best), it is understandable why the Mg-spinel was not detected, even with high-quality near-infrared spectra (e.g., Hawke et al., 2003). Although no pyroxene-bearing lithology is detected in the Hansteen Alpha structure itself, the hill is surrounded by basalts that are rich in high-Ca pyroxene. A small crater in highlands to the north-west exhibits minor low-Ca pyroxene common to highland areas. Similar spectral data for the OH-rich Compton-Belkovich region (Petro et al., 2013; Bhattacharya et al., 2013) are provided in Figures S21 and S22. Although only measured during one optical period, Compton-Belkovich exhibits a single small area that meets the criteria for the presence of Mg-spinel. All other areas across Compton-Belkovich are relatively featureless except for a remarkably strong OH/H2O feature at longer wavelengths.

5.2 Other Compositions of Spinel

Immediately following the original detection of Mg-spinel at Moscoviense (Pieters et al., 2010), the M^3 data collection was searched at low resolution for any additional regions with a strong absorption near 2000 nm and without a feature near 1000 nm. Even though thermal removal corrections had not yet been developed for M^3 data, the Sinus Aestuum region was quickly identified (#1.5 in Table 2) as surface material bearing some form of spinel, and that the spinel was only associated with the regional pyroclastic deposits of this area and not at other regional pyroclastic deposits (Sunshine et al., 2010). However, it was also readily recognized that the characteristics of these materials were quite different from the Mg-spinel observed elsewhere. The Sinus Aestuum exposures were not only very dark and widely distributed regionally, but their spectral character at shorter wavelengths suggested a different composition (Sunshine et al., 2010).

Shown in **Figure 23** are recently processed M^3 reflectance images and rock-type color-composites similar to Figure 3 across the Sinus Aestuum region. Spectra for individual pixels from two optical periods are shown for comparison in **Figure 24**. Recall that only areas with the most prominent absorption features are highlighted in the color-composite image. Undisturbed soils in the pyroclastic region are dark and essentially featureless. Pyroclastic material exposed on slopes or at any size crater exhibit the prominent 2000 nm feature. Large craters such as the one in the lower-right of the image (SA spectra 4, 5, 6, 7), exhibit mixtures of basalt and pyroclastic material. Although the presence of the second spinel band is not readily detected in these M^3 data, laboratory spectra of terrestrial spinels, including chromite, that are relatively Fe-rich typically do not exhibit sufficient spectral contrast at 2400 nm, in order to distinguish the second spinel band (e.g., Cloutis et al., 2004). We thus include this region as one exhibiting the presence of spinel, but recognize that the composition is likely to be significantly different from the widely distributed feldspathic Mg-spinel-bearing lithologies.

The Sinus Aestuum region was recently examined further by Yamamoto et al. (2013), using data from the Spectral Profiler on Kaguya, and some of the spatial relations across the region were examined further by Sunshine et al., (2014). Yamamoto et al. (2013) identified the strong 2000 nm absorption and focused on a more detailed assessment of the short wavelength features comparing them with the Cloutis et al. (2004) laboratory spinel data. They concluded that the Sinus Aestuum deposits contain a Fe/Cr-rich spinel that is distinct from Mg-spinels seen elsewhere. Since terrestrial spinels contain various amounts of ferric iron (e.g. Cloutis et al., 2004), the origin of features observed at the short wavelengths can be ambiguous. Nevertheless, recent experimental results for a suite of spinels produced under lunar-like oxygen fugacity with a range of compositions (Jackson et al., 2014) indicate that the visible features documented at Sinus Aestuum by Yamamoto et al. (2013) are consistent with relatively high concentrations of octahedral ferrous iron, which may reflect rapid cooling and/or higher bulk iron concentrations for these spinel-bearing deposits.

6 Discussion and Implications

A summary overview and comparison of M^3 confirmed areas containing PSA from diverse lunar settings evaluated in Sections 4 and 5 are presented in **Figure 25**. Several first-order observations about Mg-spinel on the Moon can be derived from the integrated data discussed here. We present a model of formation and distribution that is consistent with these data and look forward to continued progress as additional experimental and observational data become available.

6.1 General Conclusions

The global visible-to-near-infrared imaging spectroscopy data provided by M^3 on the Indian Chandrayaan-1 lunar orbiter enabled discovery of an entirely 'new' lunar rock-type – PSA, pink-spinel anorthosite. The M^3 data also enable the scale and geologic setting for this Mg-spinel-bearing lithology to be evaluated, and the results provide both new insights as well as new questions about the character and evolution of the lunar crust.

First, the occurrence of feldspathic Mg-spinel lithology (PSA) is widespread and occurs on both the nearside and the farside of the Moon. This indicates that its formation is part of the normal evolution of the lunar crust and not tied to singular events nor any specific terrain.

Second, the Mg-spinel lithology occurs only as small exposures, typically less than a few 100 m in extent, embedded in a feldspathic matrix. This suggests that the processes that produced this composition (although common) act on a relatively local scale, and are either part of or contiguous with the anorthositic crust.

Third, the distribution of Mg-spinel-bearing PSA occurrences is not random, however, and provides constraints on the origin of this unusual lithology (see section 6.2). The mineral associations that occur with or near the Mg-spinel lithology as well as the geologic and geophysical context are also important conditions.

Fourth, although not discussed explicitly here, experimental constraints on spinel produced under lunar conditions indicate that the composition of the lunar spinel identified and mapped here is notably Mg-rich (Jackson et al., 2014) based on the absence of significant features near 1000 nm or shorter wavelengths.

6.2 Implications for the Lunar Crust

From the distribution of Mg-spinel exposures seen in Figure 6, there is an apparent lack of exposures in areas of thick crust. As discussed below, most occurrences are either directly or indirectly associated with areas of thin crust.

Exposures associated with the inner ring of four basins that have tapped into the lower crust provide the most valuable constraints. The Mg-spinel exposures at 1-Moscoviense and 18-Montes Teneriffe occur directly on an uplifted inner ring, whereas the Mg-spinel exposures at 2-Theophilus and 14-Thomson were exposed by later impacts onto the inner ring. This observed geologic context strongly suggests that Mg-spinel was an inherent part of the basin ring when the ring formed, and therefore part of the pre-impact target. This not only indicates that Mg-spinel is of a deep-seated origin, but also that it predates the basin-forming era.

Distribution of Mg-spinel occurrences observed at locations dispersed in large crater walls (D) or as knobs in central peaks (K) are less directly linked to bedrock, but may be attributed to re-exposure of materials in the mega-regolith that were originally excavated and deposited by earlier basins that tapped the deep crust. The large craters exhibiting Mg-spinel exposures (D and K occurrences) post-date the basin-forming period.

Compositions associated with the occurrence of Mg-spinel-bearing PSA are relatively consistent (see summary in Table 2). In addition to the always-present feldspathic host, minor amounts of low-Ca pyroxene (LCP) or olivine may be present nearby. Small exposures of LCP are common and olivine less so. Almost never are these other mafic minerals close enough to be considered contiguous with the Mg-spinel. Instead, they are usually widely dispersed. The LCP is relatively abundant throughout the entire mega-regolith (e.g., Pieters 1986; 1993, Nakamura et al., 2013). Thus, we infer that these minerals (Mg-spinel, LCP, olivine) are all components of the lower crust, but since they are not found together, it is likely that they do not share the same origin (such as a fractionated pluton).

6.3 Inferences

There are a number of possible petrologic models for the origin of Mg-spinel on the Moon (e.g. Gross and Treiman 2011; Taylor and Pieters, 2013; Yue et al., 2013; Vaughan et al. 2013). Our preference is for one of the more simple that involves an ancient high-Mg# magma interacting with the deeper parts of an anorthositic crust to produce Mg-spinel (Prissel et al. 2012; 2013; 2014). This has the particular advantage of being consistent with the scale of the exposures, their occurrence in a very feldspathic environment, and their likely ancient age of formation. The Prissel et al. (2014) model might also accommodate a few of the exposures found as knobs in central peaks in young craters with extensive impact melt. Specifically, if the geologic context of the impact can produce high-Mg#, aluminum-rich melt (either through reworking of Mg-rich plutonic rocks or mixing Mg-rich basaltic materials with feldspathic crust), then petrologic conditions could occur similar to those proposed for the lower crust, but at low pressure. The Mg-spinel-bearing knobs at Tycho and Copernicus are surrounded by extensive impact melt and are prime candidates for this alternate mode of origin.

Certain special areas (S) of Mg-spinel exposure merit further discussion. The two associated with floor-fractured craters (S-10 and 17) could simply be chance occurrences with this landform, in which case they would be reclassified as 10-D and 17-K. Alternatively, since such craters are believed to represent areas where magma has formed a lens below the floor (e.g., Jozwiak et al., 2013), there might be a mechanism to allow melt-rock interactions to form the Mg-spinel. More detailed analyses of these areas may provide a definitive categorization. The two areas of proposed non-mare volcanism (S-25 and s-26) are most intriguing, particularly since they raise the possibility of a direct link to the source region without requiring a basin-scale impact. These areas have been hypothesized to be highly silicic from the three-band DIVINER estimates (Glotch et al. 2010; Jolliff et al. 2011). Nevertheless, little is definitive about the origin of many of these unusual regions; S-25 might simply be a lone block of lower crust that was relocated to its present position by an unknown early event, and the single exposure at s-26 (without independent confirmation) may be spurious.

Lastly, the enormous South Pole-Aitken basin continues to defy easy descriptions. There is only a single region containing Mg-spinel confirmed in SPA (14-Thomson). We have searched Schrodinger and Apollo basins, which may occur in a similar relation to SPA as Thomson/Ingenii, but have found no definite Mg-spinel candidates. If the vast terrain of feldspathic materials to the north of SPA contains SPA ejecta (as projected), it also appears devoid of Mg-spinel. As discussed above, our principal clue is that Thomson occurs within the relatively small Ingenii basin, which is itself a small mascon basin within SPA. As models continue to be proposed and tested, perhaps the origin of this Mg-spinel in SPA has nothing to do with exposure by SPA, and instead post-dates SPA but pre-dates the rest of the lunar basins, including Ingenii and the other mascon basins. That would point to a major event early in lunar history prior to the late heavy bombardment that significantly affected the mineral composition of the lower crust. Indeed, there are *many* such mysteries awaiting further data and detailed investigations.

Acknowledgments

This study was undertaken through support from the NASA LASER program under Contract #NNX12AI96G and the NASA Lunar Science Institute under Contract #NNA09DB34A.

References

Bhattacharya, S., Chauhan, P., Ajai, A. (2012) Discovery of orthopyroxene-olivine-spinel assemblage from the lunar nearside using Chandrayaan-1 Moon Mineralogy Mapper data. Current Science, vol 103, No. 1, 21-23.

Bhattacharya, S., Saran, S., Dagar, A. Chauhan, P., Chauhan, M., Ajai, A. and Kumar, S. K. (2013) Endogenic water on the Moon associated with non-mare silicic volcanism: implications for hydrated lunar interior. Current Science, vol. 105, no. 5, 685-691.

Blewett, D.T., Coman, E.I., Hawke B.R., Gillis-Davis, J.J., Purucker, M.E., and Hughes, C. G. (2011) Lunar swirls: Examining crustal magnetic anomalies and space weathering trends, Journal of Geophysical Research, 116, E02002, doi:10.1029/2010JE003656

Boardman, J.W., Pieters, C.M., Green, R.O., Lundeen, S.R., Varanasi,P., Nettles, J., Petro N., Isaacson, P., Besse, S., and Taylor, L. A. (2011) Measuring moonlight: An overview of the spatial properties, lunar coverage, selenolocation, and related Level 1B products of the Moon Mineralogy Mapper. Journal of Geophysical Research, 116, E00G14, doi:10.1029/2010JE003730.

Burns, R. G. (1993) Mineralogical applications of crystal-field theory, 2nd Edition, Cambridge University Press, Cambridge, UK, pp. 575.

Chauhan, M., Bhattacharya, S., Chauhan, P. (2014) New Locations of Fe-Mg-spinel-bearing Lithologies on the Moon as Revealed by Chandrayaan-1 Moon Mineralogy Mapper (M3) Observations, Lunar and Planetary Science Conference 45, #1829.

Cheek, L.C., Donaldson Hanna, K.L., Pieters, C.M., Head, J. W., and Whitten, J.L. (2013) The distribution and purity of anorthosite across the Orientale basin: New perspectives from Moon Mineralogy Mapper data, Journal of Geophysical Research Planets, 118, doi:10.1002/jgre.20126.

Cheek, L.C., and Pieters, C.M. (2014) Reflectance spectroscopy of plagioclase and mafic mineral mixtures: Implications for characterizing lunar anorthosites remotely, American Mineralogist, this special issue.

Clark, R. N., Swayze, G. A., Livo, K. E., Kokaly, R. F., Sutley, S. J., Dalton, J. B., McDougal, R. R., and Gent, C. A. (2003) Imaging spectroscopy: Earth and planetary remote sensing with the USGS Tetracorder and expert systems, Journal of Geophysical Research, 108(E12), 5131, doi:10.1029/2002JE001847.

Clark, R.N., Pieters, C.M., Green, R.O., Boardman, J.W., and Petro, N.E. (2011) Thermal removal from near-infrared imaging spectroscopy data of the Moon, Journal of Geophysical Research, 116, E00G16, doi:10.1029/2010JE003751

Cloutis, E.A., Sunshine, J.M., Morris, R.V. (2004) Spectral refectance-compositional properties of spinels and chromites: Implications for planetary remote sensing and geothermometry, Meteoritics & Planetary Science, 39, Nr 4, 545-565.

de Hon, R.A. (1979) Structural model of the Imbrium basin, Proc. Lunar and Planetary Science Conference, 10, 271-273.

Dhingra, D. and Pieters, C.M. (2011) Mg-Spinel rich lithology at crater Copernicus. Annual Meeting of the Lunar Exploration Analysis Group, # 2024.

Dhingra, D., Pieters, C.M., Boardman, J., Head, J.W. III, Isaacson, P.J., Taylor, L.A., and the M3 Team (2011a) Theophilus Crater: Compositional Diversity and Geological Context of Mg-Spinel Bearing Central Peaks, Lunar and Planetary Science Conference, XLII, #2388.

Dhingra D., Mustard, J.F., Wiseman, S., Pariente, M., Pieters, C.M. and Isaacson, P.J. (2011b) Non-linear spectral unmixing using Hapke modeling: Application to remotely acquired M3 spectra of spinel bearing lithologies on the Moon, Lunar and Planetary Science Conference. *XLII*, # 2431

Dhingra, D., Pieters, C.M., Boardman, J.W., Head, J.W., Isaacson, P.J., and Taylor, L.A. (2011c) Compositional diversity at Theophilus crater: Understanding the geologic context of Mg-spinel bearing central peaks, Geophysical Research Letters, 38, doi:10.1029/2011GL047314.

Donaldson Hanna, K (2013) Compositional Diversity of the Moon's Anorthositic Crust: Integrating Remote Observations with Laboratory Measurements of Analogue Materials under Simulated Lunar Conditions, PhD Thesis, Brown University, pp 306.

Donaldson Hanna, K. et al., (2014) Global Assessment of Pure Crystalline Plagioclase across the Moon and Implications for Evolution of the Primary Crust, in review Journal of Geophysical Research.

Glotch, T. D., Lucey, P.G., Bandfied, J.L., Greenhagen, B.T., Thomas, I.R., Elphic, R.C., Bowles, N., Wyatt, M.B., Allen, C.C., Donaldson Hanna, K., and Paige, D. A. (2010) Highly silicic compositions on the Moon, Science, 329, doi:10.1126/science.1192148

Green, R.O., et al. (2011) The Moon Mineralogy Mapper (M^3) Imaging spectrometer for lunar science: Instrument description, calibration, on-orbit measurements, science data calibration and on-orbit validation. Journal of Geophysical Research, 116, E00G19, doi:10.1029/2011JE003797.

Gross, J., and Treiman, A.H. (2011) Unique spinel-rich lithology in lunar meteorite ALHA 81005: Origin and possible connection to M3 observations of the farside highlands, Journal of Geophysical Research, 116, E10009, doi:10.1029/2011JE003858.

Haggerty, S.E. (1978) Luna 24: Systematics in spinel mineral chemistry in the context of an intrusive petrogenetic grid, in Mare Crisium: The View from Luna 24, Pergamon Press (Merrill and Papike Eds.) 523-535.

Haruyama, J., et al., (2009) Long-Lived Volcanism on the Lunar Farside Revealed by SELENE Terrain Camera, Science, 323, 905-908.

Hapke, B. (2001) Space weathering from Mercury to the asteroid belt, Journal of Geophysical Research, 106, E5, 10039-10073.

Hawke, B. R., Peterson, C.A., Blewett, D.T.,. Bussey, D.B.J, Lucey, P.G., Taylor, G.J., and Spudis, P.D. (2003a) Distribution and modes of occurrence of lunar anorthosite, Journal of Geophysical Research, 108(E6), 5050, doi:10.1029/2002JE001890.

Hawke, B. R., Lawrence, D.J., Blewett, D.T., Lucey, P.G., Smith, G.A., Spudis, P.D., and Taylor, G.J. (2003b) Hansteen Alpha: A volcanic construct in the lunar highlands, Journal of Geophysical Research, 108(E7), 5069, doi:10.1029/2002JE002013.

Head, J. W. (2010) Transition from complex craters to multi-ringed basins on terrestrial planetary bodies: Scale-dependent role of the expanding melt cavity and progressive interaction with the displaced zone, Geophysical Research Letters, 37, L02203, doi:10.1029/2009GL041790.

Ishihara, Y., Goossens, S., Matsumoto, K., Noda, H., Araki, H., Namiki, N., Hanada, H., Iwata, T., Tazawa, S., and Sasaki, S. (2009) Crustal thickness of the Moon: Implications for farside basin structures, Geophysical Research Letters, 36, L19202, doi:10.1029/2009GL039708

Jackson, C.R.M., Cheek, L.C., Parman S.W., Cooper, R.F., and Pieters, C.M. (2012)

Compositional constraints on lunar spinel anorthosite: Synthesis of spinel with variable iron content, Lunar and Planetary Science Conference, XLIII, # 2335.

Jackson, C.R.M., Cheek, L.C., Parman S.W., Cooper, R.F., Pieters, C.M., and Dyar, M. D. (2014) Compositional constraints on lunar Mg-rich spinel: Synthesis of spinel with variable iron content, American Mineralogist, this special issue.

Jolliff, B. L., Gillis, J.J., Haskin, L.A., Korotev, R.L., and Wieczorek, M.A. (2000) Major lunar crustal terranes: Surface expressions and crust-mantle origins, Journal of Geophysical Research, 105, 4197 – 4216, doi:10.1029/ 1999JE001103.

Jolliff, B.L., Wiseman, S.A., Lawrence, S.J., Tran, T.N., Robinson, M.S., Sato, H., Hawke, B.R., Scholten, F., Oberst, J., Hiesinger, H., va der Bogert, C. H., Greenhagen, B.T., Glotch, T.D. and D. A. Paige (2011) Non-mare silicic volcanism on the lunar farside at Compton-Belkovich, Nature Geoscience, 4, doi:10.1038/ngeo1212

Jozwiak, L. M., Head, J.W., Zuber, M.T., Smith, D.E., and Neumann, G.A. (2012) Lunar floor-fractured craters: Classification, distribution, origin and implications for magmatism and shallow crustal structure, Journal of Geophysical Research, 117, E11005, doi:10.1029/2012JE004134.

Kaur, P., Chauhan, P., Bhattacharya, S., Ajai, and Kumar, A.S.K. (2012) Compositional Diversity at Tycho Crater: Mg-Spinel Exposures Detected from Moon Mineralogical Mapper (M3) Data, Lunar and Planetary Science Conference. 43, #1434.

Kaur, P., Chauhan, P., and Ajai (2013a) Detection of Mg-Spinel Exposures from the Anorthositic Terrain Surrounding Mare Ingenii on the Far Side of the Moon, Lunar and Planetary Science Conference. 44, #1547.

Kaur, P., Chauhan, P., and Ajai (2013b) Exposures of Mg-Spinel on an Evolved Silicic Lithology Hansteen Alpha on the Moon, Lunar and Planetary Science Conference 44, #1348.

Kaur, P. and Chauhan, P. (2014) Detection of Spinels Exposures from some Near Side Locations of the Moon, Lunar and Planetary Science Conference 45, #2059.

Klima, R. L., Pieters, C.M., and Dyar, M.D. (2007) Spectroscopy of synthetic Mg-Fe pyroxenes I: Spin-allowed and spin-forbidden crystal field bands in the visible and near-infrared, Meteoritics and Planetary Science, 42, 235-353, doi:10.1111/j.1945-5100.2007.tb00230.x

Klima, R.L., Dyar, M.D., and Pieters, C.M. (2011) Near-infrared spectra of clinopyroxenes: Effects of Ca content and crystal structure, Meteoritics and Planetary Science, 46, 379-395, doi: 10.1111/j.1945-5100.2010.01158.x

Kramer, G.Y., Besse, S., Dhingra, D., Nettles, J.W.W., Klima, R.L.P., Garrick-Bethell, I., Clark, R.N.N., Combe, J.P., Head, J. W., Taylor, L.A.A., Pieters, C.M.M., Boardman, J.W., and McCord, T. B. (2011) M^3 Spectral Analysis of Lunar Swirls and the Link between Optical Maturation and Surface Hydroxyl Formation at Magnetic Anomalies, Journal of Geophysical Research, 116, E00G18, doi:10.1029/2010JE003729

Lal, et al., (2011) Identification of spinel group of minerals on central peak of crater Theophilus, Lunar and Planetary Science Conference 42, # 1339.

Lal, D., Chauhan, P., Shah, R. D., Bhattacharya, S., Ajai and Kirankumar, A.S. (2012) Detection of Mg spinel lithologies on central peak of crater Theophilus using Moon Mineralogy Mapper (M3) data from Chandrayaan-1, Journal of Earth System Science, 121(3), 847-853

Lundeen, S., McLaughlin, S., Alanis, R. (2011) Moon Mineralogy Mapper Data Product Software Interface Specification. PDS document Version 9.10, Jet Propulsion Laboratory, JPL D-39032, Pasadena, CA.

Nakamura, et al. (2012) Compositional evidence for an impact origin of the Moon's Procellarum basin, Nature Geoscience,| published online 28 October, DOI: 10.1038/NGEO1614

Ohtake, M., Matsunaga, M.T., Haruyama, J., Yokota, Y., Morota, T., Honda, C., Ogawa, Y., Torii, M., Miyamoto, H., Arai, T., Hirata, N., Iwasaki, A., Nakamura, R., Hiroi, T., Sugihara, T., Takeda, H., Otake, H., Pieters, C.M., Saiki, K., Kitazato, K., Abe, M., Asada, N., Demura, H., Yamaguchi, Y., Sasaki, S., Kodama, S., Terazono, J., Shirao, M., Yamaji, A., Minami, S., Akiyama, H., and Josset, J.L. (2009) The global distribution of pure anorthosite on the Moon, Nature, 461, 236-240, doi:10.1038/nature08317.

Ohtake, M., Pieters, C.M., Isaacson, P.J., Besse, S., Yokota, Y., Matsunaga, T., Boardman, J., Yamamoto, S., Haruyama, J., Staid, M., Mall, U., Green, R., and Sunshine, J. (2013) One Moon, Many Measurements 3: Spectral reflectance, Icarus, 226, 364-374.

Petro, N. E., Isaacson, P. J. , Pieters, C. M., Jolliff, B. L., Carter, L. M., and Klima, R. L. (2013) Presence of OH/H2O associated with the lunar Compton-Belkovich volcanic complex identified by the Moon Mineralogy Mapper (M3), Lunar and Planetary Science Conference*, XLIV,* # 2688.

Pieters, C.M. (1986) Composition of the lunar highland crust from near-infrared spectroscopy, Reviews of Geophysics, 24, 557-578

Pieters, C.M., Taylor, L.A., Noble, S.K., Keller, L.P., Hapke, B., Morris, R.V., Allen, C.C., McKay, D.S., and Wentworth, S. (2000) Space weathering on airless bodies: Resolving a mystery with lunar samples, Meteoritics and Planetary Science, 35, 1101-1107.

Pieters, C.M., Boardman, J., Buratti, B., Chatterjee, A., Clark, R., Glavich, T., Green, R., Head, J. III, Isaacson, P., Malaret, E., McCord, T., Mustard, J., Petro, N., Runyon, C., Staid, M., Sunshine, J., Taylor, L., Tompkins, S., Varanasi, P., and White, M. (2009) The Moon Mineralogy Mapper (M^3) on Chandrayaan-1, Current Science, 96, 500-505.

Pieters, C.M., Boardman, J., Buratti, B., Clark, R., Combe, J.-P., Green, R., Goswami, J.N., Head, J.W. III, Hicks, M., Isaacson, P., Klima, R., Kramer, G., Kumar, K., Lundeen, S., Malaret, E., McCord, T.B., Mustard, J., Nettles, J., Petro, N., Runyon, C., Staid, M., Sunshine, J., Taylor, L.A., Thaisen, K., Tompkins, S., Varanasi, P. (2010) Identification of a new spinel-rich lunar rock type by the Moon Mineralogy Mapper (M3), Lunar and Planetary Science Conference 41, #1854.

Pieters, C.M., Besse, S., Boardman, J., Buratti, B., Cheek, L., Clark, R.N., Combe, J.P., Dhingra, D., Goswami, J.N., Green, R.O., Head, J.W., Isaacson, P., Klima, R., Kramer, G., Lundeen, S., Malaret, E., McCord, T., Mustard, J., Nettles, J., Petro, N., Runyon, C., Staid, M., Sunshine, J., Taylor, L.A., Thaisen, K., Tompkins, S., and Whitten, J. (2011) Mg-spinel lithology: A new rock type on the lunar farside, Journal of Geophysical Research, 116, E00G08, doi:10.1029/2010JE003727

Pieters, C.M., Boardman, J., Ohtake, M., Matsunaga, T., Haruyama, J., Green, R.O., Mall, U., Staid, M., Isaacson, P.J., Yokota, Y., Yamamoto, S., Besse, S., and Sunshine, J. (2013a) One Moon, Many Measurements 1: Radiance values, Icarus, 226, 951-963.

Pieters C.M., Donaldson Hanna, K., Cheek, L., Dhingra, D., Moriarty, D., Parman, S., Jackson, C., Prissel, T., (2013b) Compositional Evolution of the Early Lunar Crust: Observed Diverse Mineralogy of the Upper and Lower Crust, Lunar and Planetary Science Conference 44, #2545,

Prissel, T.C., Parman, S.W., Jackson, C.R.M., Dhingra, D., Ganskow, G., Cheek, L.C., Rutherford, M.J., Hess, P.C., and Pieters, C.M. (2012) Melt-wallrock reactions on the

Moon: Experimental constraints on the formation of newly discovered Mg-spinel anorthosites, Lunar and Planetary Science Conference. Sci., XLIII, # 2743.

Prissel, T. C., Parman, S.W., Head, J.W. III, Jackson, C.R.M., Rutherford, M.J., Hess, P.C., Cheek, L.C., Dhingra, D., and Pieters, C.M. (2013) An "uncollected" member of the Mg-suite: Mg-Al pink spinel anorthosites and their place on the Moon, Lunar and Planetary Science Conference. Sci., XLIV, # 3066.

Prissel, T.C., Parman,, S.W. Jackson, C.R., Rutherford, M.J., Hess, P.C., Head, J.W., Cheek, L., Dhingra, D., and Pieters, C.M. (2014), Pink Moon: The petrogenesis of pink spinel anorthosites and implications concerning Mg-suite magmatism, *submitted to: Earth Planetary Science Letters.*

Robinson, M. S., Brylow, S. M., Tschimmel, M., Humm, D., Lawrence, S. J., Thomas, P. C., Denevi, B. W., Bowman-Cisneros, E., Zerr, J., Ravine, M. A., Caplinger, M. A., Ghaemi, F. T., Schaffner, J. A., Malin, M. C., Mahanti, P., Bartels, A., Anderson, J., Tran, T. N., Eliason, E. M., McEwen, A. S., Turtle, E., Joliff, B. L., and Hiesinger, H., (2010) Lunar Reconnaissance Orbiter Camera (LROC) Instrument Overview, Space Science Review, 150, 81-124, doi:10.1007/s11214-010-9643-2.

Schultz, P.H. (1976) Floor-fractured lunar craters, Moon, 15, 241–273, doi:10.1007/BF00562240.

Smith, D. E., Zuber, M. T., Neumann, G. A., Lemoine, F. G., Mazarico, E., Torrence, M. H., McFarry, J. F., Rowlands, D. D., Head III, J. W., Duxbury, T. H., Aharonson, O., Lucey, P. G., Robinson, M. S., Barnouin, O. S., Cavanaugh, J. F., Sun, X., Liiva, P., dan Mao, D., Smith, J. C., and Bartels, A. E., (2010) Initial observations from the Lunar Orbiter Laser Altimeter (LOLA), Geophysical Research Letters, 37, doi:10.1029/2010GL043751.

Spudis, P.D. (1993) The geology of multi-ring impact basins, Cambridge University Press, Cambridge, UK, pp. 277.

Srivastava, N. and Gupta, R.P. (2012) Compositional diversity inside Lowell Crater, Orientale Basin: Evidences for extensive spinel rich deposits, 2d Conference on Lunar Highlands Crust, LPI, #9016.

Srivastava, N. and Gupta, R.P. (2013) Spatial distribution of spinel in the Orientale Basin: New insights from M3 data, Lunar and Planetary Science Conference 44 #1509.

Sun, Y., Lin, L., and Zhang, Y.Z. (2013) Detection of Mg-spinel bearing central peaks using M3 images, Lunar and Planetary Science Conference 44, #1393

Sunshine, J.M., Besse, S., Petro, N.E., Pieters, C.M., Head, J.W., Taylor, L.A., Klima, R.L., Isaacson, P.J., Boardman, J.W., Clark, R. and the M3 Team. (2010) Hidden in plain sight: Spinel-rich deposits on the nearside of the Moon as revealed by Moon Mineralogy Mapper (M3), Lunar and Planetary Science Conference 41, #1508

Sunshine, J.M., Petro, N.E., Besse, S., and Gaddis, L.R. (2014), Widespread exposures of small scale spinel-rich pyroclastic deposits in Sinus Aestuum, Lunar and Planetary Science Conference 44, #2297.

Taylor, L.A., and Pieters, C.M., 2013, Pink-Spinel Anorthosite formation: Considerations for a feasible petrogenesis, Lunar and Planetary Science Conference 44, #2785.

Vaughan et al., (2013) Geology and petrology of enormous volumes of impact melt on the Moon: A case study of the Orientale basin impact melt sea, Icarus, doi: http://dx.doi.org/10.1016/j.icarus.2013.01.017

Wieczorek, M.A., Neumann, G.A., Nimmo, F., Kiefer, W.S., Taylor, G.J., Melosh, H.J., Phillips, R.J., Solomon, S.C., Andrews-Hanna, J.C., Asmar, S.W., Konopliv, A. S., Lemoine, F.G., Smith, D.E., Watkins, M.M., Williams, J.G., and Zuber, M.T., (2012) The crust of the Moon as seen by GRAIL, Science, doi:10.1126/science.1231530.

Yamamoto, S., Nakamura, R., Matsunaga, T., Ogawa, Y., Ishihara, Y., Morota, T., Hirata, N., Ohtake, M., Hiroi, T., Yokota, Y., and Haruyama, J. (2013) A new type of pyroclastic deposit on the Moon containing Fe-spinel and chromite, Geophysical Research Letters, doi: 10.1002/grl.50784.

Yue, Z., Johnson, B.C., Minton, D.A, Melosh, H.J., Ki, K., Hu, W., and Liu, Y. (2013) Projectile remnants in central peaks of lunar impact craters, Nature Geoscience, Published online 26 May, 435-437.

Tables

Table 1. Spectral Parameters used to produce the enhanced color-composite of Figure 3 and subsequent figures. R_{NNN} is M^3 Level 2 reflectance at NNN wavelength in nm. ENVI is the image processing software used.

Mineral Link	General Formulation	ENVI Band Math	RGB
Pyroxene Ratio	$(R_{700} + R_{1200})/2*R_{950}$	float((b7+b32)/b19)	Red
Spinel Ratio	R_{1400}/R_{1750}	float((b42+b43)/(b54+b55))	Green
PAN Ratio	$(R_{1000} + R_{1500})/2*R_{1250}$	float((b22+b47)/b34)	Blue

Table 2. Summary of areas confirmed to contain spinel. The # indicates the approximate order first identified by the Reference given. Confirmed spinel-bearing areas are classified by Type: B-Basin ring; D-Dispersed in wall or ejecta; K-Knobs in crater; S-Special (floor fractured craters, possible highland volcanism); P-Pyroclastic deposits. Lower case classification indicates tentative assignment and only one measurement; *^° indicates files that contain more than one target; Mineral abbreviations: Sp-spinel; LCP-low-Ca pyroxene; Ol-olivine; Xl-Plag-crystalline plagioclase; CPX-high-Ca pyroxene.

[See Table 2 below]

Table 2 References: 1) Pieters et al., 2010; 2) Sunshine et al., 2010; 3) Pieters et al., 2011; 4) Dhingra et al., 2011a; Dhingra et al., 2011c; 5) Lal et al., 2011; Lal et al., 2012; 6) Dhingra and Pieters 2011; 7) Kaur et al., 2012; 8) Bhattacharya et al., 2012; 9) Donaldson Hanna 2013; --personal communication; 10) Pieters et al., 2013b; 11) Kaur et al. 2013a; 12) Kaur et al., 2013b; 13) Yamamoto et al., 2013; 14) Sun et al., 2013; 15) Pieters personal communication; 16) Bhattacharya et al., 2013; 17) Kaur and Chauhan, 2014.

Table 2.

#	Type	Name	Lat	Long	M3 Files	OP	Ref	Other Minerals?	Location of Sp, comments
8	K	Albategnius	-11.4	3.5	M3G20090109T022525**	OP1Aw	9	LCP nearby	sm knob off central peak
					M3G20090205T092400	OP1Bc			
					M3G20090608T083142	OP2Cw			
26	s	Compton-Belkovi	61.3	99.9	M3G20090601T064032	OP2Cw	16	strongly hydrated	single knob
3	K	Copernicus	8.9	-19.5	M3G20090207T044515	OP1Bc	6	Ol,	sm knob off central peaks
					M3G20090416T122951	OP2Ac			
					M3G20090513T191408	OP2Bw			
17	S	Dalton	17.1	-84.5	M3G20090115T174705	OP1Aw	9	faint Xl Plag	FFCr; sp in CP
					M3G20090212T024412	OP1Bc			
					M3G20090421T082045	OP2Ac			
					M3G20090712T093119	OP2Cc			
6	D	Endymion	52.0	55	M3G20090201T104533	OP1Bc	8	tr LCP	S wall; crater mare filled
					M3G20090604T104552	OP2Cw			
					M3G20090729T022657	OP2Cc			
23	K	Eudoxus	44.1	16.6	M3G20090204T134332°°	OP1Bc	14	abundant LCP	single; tiny Sp
					M3G20090607T073505	OP2Cw			
21	D	Geminus	34.5	56.6	M3G20090201T085853	OP1Bc	9	Ol, [LCP in CP]	Complex, along wall; N, W, S
					M3G20090604T064302	OP2Cw			
					M3G20090729T022657	OP2Cc			
24	K	Goodacre	-32.6	14.2	M3G20090204T134332°°	OP1Bc	15	tr LCP	knob end of crater chain
					M3G20090607T153144	OP2Cw			
25	S	Hansteen Alpha	-12.4	-50.4	M3G20090418T190900	OP2Ac	12	nothing detected	multiple discrete exposures
					M3G20090612T101600	OP2Cw			
13	k	Joliot	25.9	93.4	M3G20090601T145212	OP2Cw	9	Xl-Plag; CPX - mare	sm knob of Pk; mare nearby
20	K	Macrobius	21.3	46.1	M3G20090105T194305	OP1Aw	9	Ol, LCP	Mixed peaks, knobs
					M3G20090202T042831	OP1Bc			
					M3G20090605T040250	OP2Cw			
					M3G20090729T185951	OP2Cc			
18	B	Montes Teneriffe	47.1	-11.8	M3G20090206T185050	OP1Bc	9	nothing detected	2 sm exposures; Imbrium ring
					M3G20090415T222023^	OP2Ac			
					M3G20090609T183254*	OP2Cw			
1	B	Moscoviense	24.7	143.4	M3G20081229T101650	OP1Aw	1, 3	Ol, LCP	First detection; inner ring
					M3G20090125T172601	OP1Bc			
16	D	Piccolomini	-28.0	32	M3G20090203T041059°	OP1Bc	9	tr LCP [wall only]	wall; CP is Xl Plag
					M3G20090203T080104	OP1Bc			
					M3G20090606T053022^^	OP2Cw			
10	S	Pitatus	-29.8	-13.6	M3G20090206T145451	OP1Bc	9	nothing detected	S Cr wall only; mare filled FFCr
					M3G20090609T183254*	OP2Cw			
15	k	Simpelius	-69.9	16	M3G20090607T110414	OP2Cw	9	LCP	central knob
1.5	P	Sinus Aestuum	-5.8	-9.6	M3G20090206T084850	OP1Bc	2, 13	[Fe,Cr-spinel]	regional Dark Mantling Material
					M3G20090609T101951	OP2Cw			
					M3G20090609T183254*	OP2Cw			
27	B	Sinus Iridum	41.4	-36.2	M3G20090208T100012	OP1Bc	17	nothing detected	small areas; Ol < 200km NE
					M3G20090417T155652	OP2Ac			
					M3G20090611T090220	OP2Cw			
12	K	Stiborius	-35.0	32	M3G20090203T041059°	OP1Bc	9	near LCP	central knob
					M3G20090203T061431	OP1Bc			
					M3G20090606T053022^^	OP2Cw			
					M3G20090730T204211	OP2Cc			
2	B	Theophilus	-11.5	26.1	M3G20090203T160452	OP1Bc	4, 5	Xl Plag. Ol?	CP; LCP in N wall; Nectaris ring
					M3G20090731T045352	OP2Cc			
14	B	Thomson	-32.7	166	M3G20090623T052831	OP2Cw	9,10,11	tr LCP, Ol	many wall exposures; SPA ring
					M3G20090623T095551	OP2Cw			
					M3G20090623T135841	OP2Cw			
					M3G20090720T173631	OP2Cc			
					M3G20090720T214000	OP2Cc			
4	K	Tycho	-43.3	-11.1	M3G20090206T105850	OP1Bc	7	LCP, HCP	CP, near melt
					M3G20090415T202222^	OP2Ac			
					M3G20090415T222023^	OP2Ac			
					M3G20090609T095022	OP2Cw			
9	D	Walther	-33.0	0.6	M3G20090205T133443	OP1Bc	9, 13	tr LCP	wall & CP
					M3G20090608T125102	OP2Cw			
7	D	Werner	-27.0	2.8	M3G20090109T022525**	OP1Aw	9	minor LCP	Rim; N ejecta
					M3G20090205T094623	OP1Bc			
					M3G20090608T083142	OP2Cw			

Figure Captions

Figure 1. Laboratory reflectance spectra of representative terrestrial spinels and lunar minerals and soil. In this and several subsequent figures with spectra, black vertical dashed lines are drawn at 1000 and 2000 nm to allow cross comparison of features. The Mg-spinel and chromite are from Cloutis et al. 2004 (SP117, CHR109). The lunar samples were measured in RELAB (plagioclase-62241 separate; olivine-72415; soil-62231; high-Ca clinopyroxene CPX-12063 separate; low-Ca orthopyroxene LCP-78235 separate). The lunar olivine shown here contains trace inclusions of chromite which add a weak feature near 2000 nm.

Figure 2. Examples of confirmed M^3 spectra for Mg-spinel (green). An example of a low-iron synthetic spinel (black, separate scale) prepared under lunar conditions is provided for comparison (Jackson et al., 2014). Arrows indicate diagnostic features of spinel discussed in the text.

Figure 3. M^3 OP1b images across Theophilus Crater. [Left] M^3 reflectance at 1489 nm retaining local geometry of illumination (*_SUP.IMG PDS data). [Right] Color-composite draped over M^3 reflectance derived from the three M^3 spectral parameters contrast stretched to only indicate the rock type dominated by: Red=pyroxene, Green=spinel, Blue=plagioclase. Arrows indicate location of spectra in Figure 4. Scale bar is 10 km. Spinel is found almost entirely within the peaks; significant pyroxene only occurs in the northern wall. Similar independent data for the later OP2c3 is provided in Figure S3.

Figure 4. Independent M^3 reflectance spectra obtained for the same areas in Theophilus Crater during two optical periods (OP) that were several months apart. Locations are shown with arrows in Figure 3. All areas except #5 are associated with the central peaks. Additional spectra across the peaks can be found in Figure S4.

Figure 5. Illustration of spectral parameters used in this analysis to highlight regions in a spatial context that contain prominent features due to specific minerals. Vertical colored lines indicate the wavelengths used for the parameters itemized in Table 1: a) Mg-spinel (green), b) Crystalline plagioclase (blue), c) Pyroxene (red). Example M^3 spectra for areas 1-6 from Fig 3a are used to illustrate features seen in M^3 data.

Figure 6. Location of areas with confirmed M^3 identification of spinel. Basemaps are (Top) Lunar Reconnaissance Orbiter Camera (LROC) Wide Angle Camera (WAC) brightness mosaic (Robinson et al. 2010); (Middle) Lunar Orbiter Laser Altimeter (LOLA) topography (Smith et al. 2010); (Bottom) The Gravity Recovery and Interior Laboratory (GRAIL) crustal thickness (Wieczorek et al. 2012). Oversized symbols are centered on the spinel exposure. Categories are discussed in the text. B: Basins; D: dispersed; K: knobs, S: Special; P: pyroclastic. Numbers (in green) are in approximate order of discovery. See Table 2 for specific information on locations.

Figure 7. Example M^3 spectra for three of the rock types exposed along the inner ring of Moscoviense basin as measured during two independent optical periods (OP1b and OP1a). Designations for areas 1, 2, 4a are those used in Pieters et al., (2011). Mg-spinel occurs at 1 (green), low-Ca pyroxene at 2 (red), and olivine at 4a (purple). A spectrum from a crater in the mare basalt to the east (MareCr) is provided for comparison (maroon) and exhibits the signature of a more Fe- and Ca-rich clinopyroxene. Color-composite images for Moscoviense similar to Figure 3 for both optical periods can be found in Figure S7.

Figure 8. LROC WAC mosaic image of northern Imbrium. Arrow indicates Montes Teneriffe. Scale bar is 100 km.

Figure 9. M^3 data for Montes Teneriffe obtained during OP1b. Left: Reflectance image. Right: Rock type color-composite (similar to Figure 3). Similar images for independent data acquired with different illumination geometry during OP2a and OP2c1 show the same spatial relations and are provided in Figure S9. Arrows indicate the location of spectra in Figure 10. Scale bar is 10 km.

Figure 10. M^3 reflectance spectra for areas in Montes Teneriffe acquired during OP1b. Spectra for the same areas acquired with different illumination geometry during OP2a and OP2c1 are provided in Figure S10 (For OP1b the second spinel area near area 1 was largely in shadow.)

Figure 11. LROC WAC mosaics providing an overview of the Nectaris region containing Theophilus (Top) and the NW portion of South Pole-Aitken basin containing Thomson/Ingenii (Bottom). Scale bar is 100 km. Small white arrow indicates Apollo 16 site.

Figure 12. Sub-sections of M^3 data for Thomson acquired during OP2c2 and prepared similar to Figure 3. Top images are the northern rim and bottom images are the southern rim. Left: Reflectance 1489 image (from SUP). Right: rock type color-composite superimposed on brightness image. Locations for representative areas 1-5 are indicated with arrows and their spectra are shown in Figure 13. (See Figure S12 for a similar mosaic of independent OP2c1 data across the full Thomson crater.) Scale bar is 10 km.

Figure 13. M^3 spectra for the same areas in Thomson acquired during independent periods OP2c1 and OP2c2. Areas along the southern rim are shown in solid lines; areas along the northern rim are in dotted lines. Although the overall spectral properties remain the same between optical periods, differences in brightness for individual areas are due to differences in illumination geometry of the measurements. Spectra for additional Thomson areas from both optical periods are shown in Figure S13

Figure 14. LROC WAC image mosaic of Albategnius (K-8). Scale bar is 10 km. Black box indicates M^3 area in Figure 15.

Figure 15. M^3 data for Albategnius (K-8) from OP1a prepared similar to Figure 3. Left: 1489 nm reflectance *SUP image. Right: Rock-type color-composite superimposed on brightness image. Arrows indicate locations of areas 1-6.

Figure 16. M^3 spectra for the representative areas shown in Figure 15 from OP1a. Independent M^3 spectra for the same areas obtained during optical period OP2c1 are provided in Figure S16 along with reflectance spectra relative to the featureless area Albategnius 5 in order to highlight subtle variations for both optical periods.

Figure 17. OP1b M^3 data for Geminus (D-21). Left: 1489 nm SUP brightness image. Right: Rock-type color-composite (similar to Figure 3 as discussed in the text) superimposed on brightness image. Arrows indicate the location of areas for which spectra were acquired and shown in Figure 18. Scale bar is 10 km.

Figure 18. M^3 spectra for representative areas in Geminus shown in Figure 17. Spectra for several of the same areas obtained during independent optical periods OP2c1 and OP2c3 are shown in Figure S18 along with spectra relative to the featureless area Wall 1 in order to allow subtle variations to be highlighted.

Figure 19. M^3 data for Dalton crater (S-17) from OP1a. Left: 1489 nm *SUP reflectance image. Right: Rock-type color-composite similar to Figure 3 superimposed on brightness image. Arrows indicate location for spectra of Figure 20. Scale bar is 10 km. Independent color-composites for three additional optical periods are presented in Figure S19.

Figure 20. M^3 spectra for areas in Dalton crater shown in Figure 19. Independent Dalton M^3 spectra for the same areas obtained during three additional optical periods with different illumination geometry are shown in Figure S20.

Figure 21. M^3 data for Hansteen Alpha (S-25). Left: 1489 nm *SUP reflectance image from OP2a. Middle: Rock-type color-composite similar to Figure 3 superimposed on brightness image for OP2a. Right: Rock-type color-composite for OP2c1. Scale bar is 10 km.

Figure 22. Independent M^3 spectra for the same areas in the Hansteen Alpha region obtained during two different optical periods with different illumination geometry. The green spectra are for four different spinel-bearing areas seen in both optical periods, the blue spectra are for three nearby feldspathic areas. The two pyroxene-bearing areas (red spectra) occur outside Hansteen Alpha and are indicated with a white arrow (low-Ca pyroxene) and a black arrow (high-Ca pyroxene in basalt) on Figure 21. Note that for OP2a the sun was relatively low (illumination angle ~60° from vertical) whereas for OP2c1 the sun was high (illumination angle ~14°). The effect of shadows on variations in measured brightness is thus more prominent for OP2a

Figure 23. M^3 data covering part of the Sinus Aestuum pyroclastic region obtained during OP2c1 prepared similar to Figure 3. [Left] 700 nm reflectance image. Arrows indicate location of spectra in Figure 24. [Right] Rock-type color-composite superimposed on reflectance image. The basaltic terrain to the west of the dark pyroclastic deposits is rich in high-Ca pyroxene. Scale bar is 10 km.

Figure 24. M^3 spectra of the same areas in the Sinus Aestuum region obtained during Optical periods OP2c1 and OP1b. SA1 represents mature soil developed on the pyroclastic deposits. SA2 represents an area of more recently exposed pyroclastic deposit near a crater and SA3 the crater interior. Areas SA4, 5, 6, 7 illustrate mixtures exposed at a ~6 km crater, and SA8 is an example of a normal CPX-rich mare crater.

Figure 25. Summary comparison of confirmed M^3 spectra of spinel found in a diversity of geologic settings discussed in the text. Top to bottom at 2100 nm: Endymion1, Endymion2, ThomsonS1, WernerWall1, Montes Teneriffe1, Moscoviense 1, ThomsonS2, TheophilusS1, TychoSp3, Sinus Aestuum2.

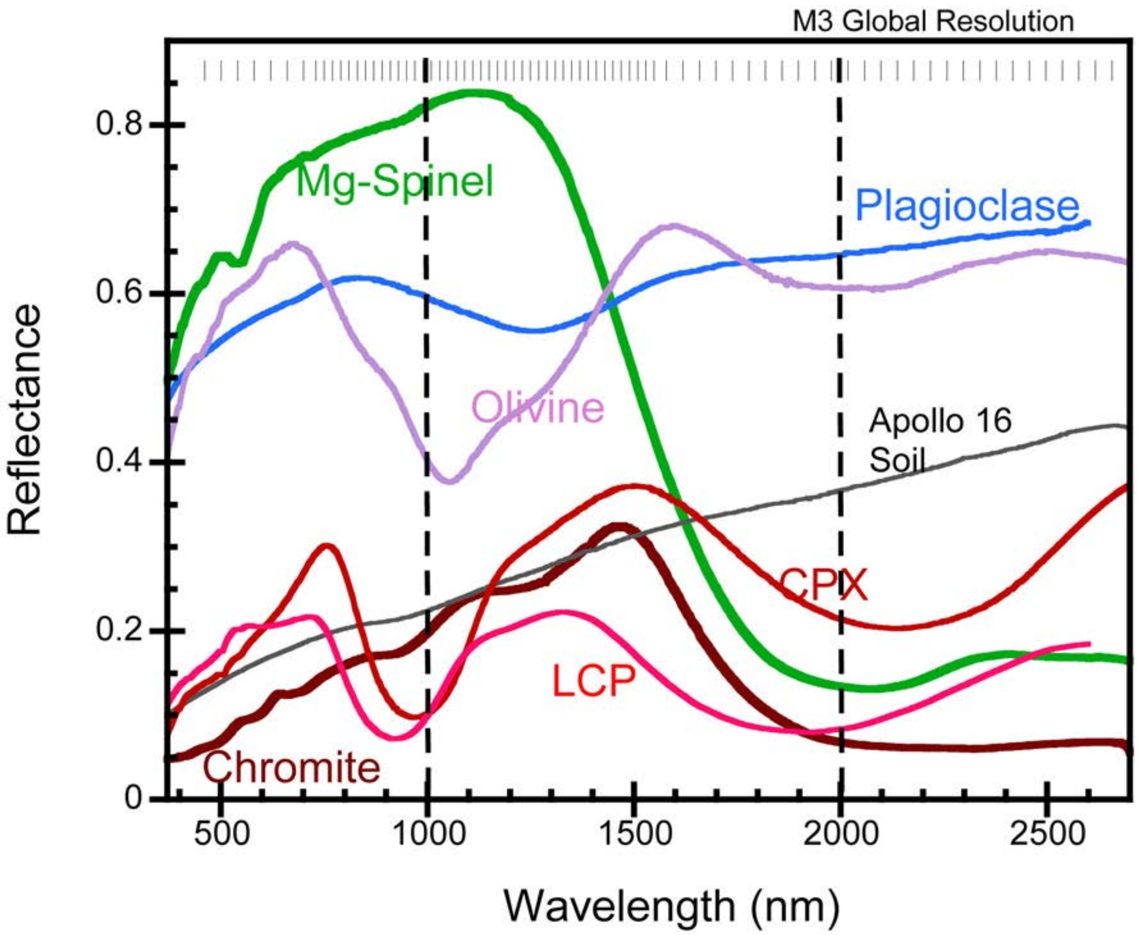

Figure 1 Laboratory reflectance spectra of representative terrestrial spinels and lunar minerals and soil. In this and several subsequent figures with spectra, black vertical dashed lines are drawn at 1000 and 2000 nm to allow cross comparison of features. The Mg-spinel and chromite are from Cloutis et al. 2004 (SP117, CHR109). The lunar samples were measured in RELAB (plagioclase-62241 separate; olivine-72415; soil-62231; high-Ca clinopyroxene CPX-12063 separate; low-Ca orthopyroxene LCP-78235 separate). The lunar olivine shown here contains trace inclusions of chromite which add a weak feature near 2000 nm.

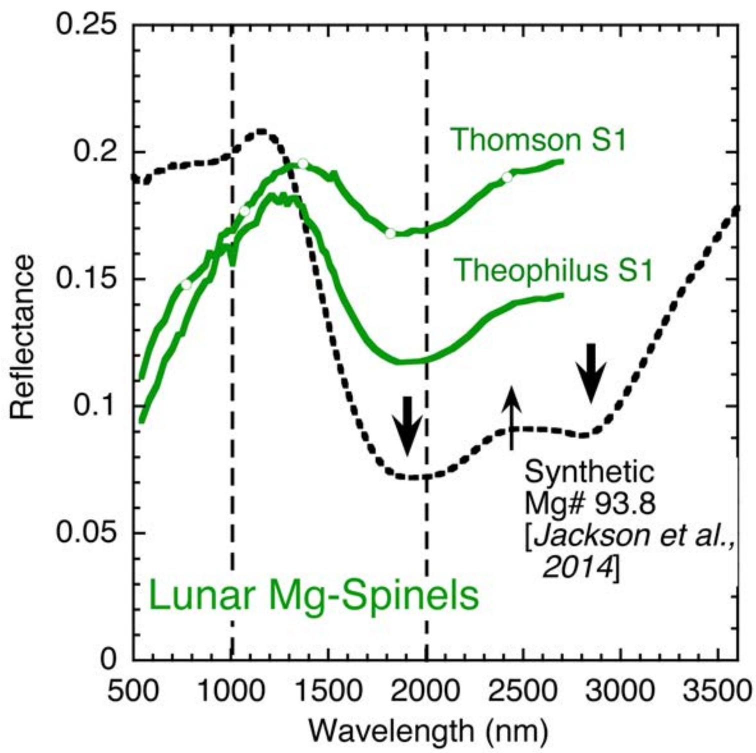

Figure 2. Examples of confirmed M^3 spectra for Mg-spinel (green). An example of a low-iron synthetic spinel (black, separate scale) prepared under lunar conditions is provided for comparison (Jackson et al., 2014). Arrows indicate diagnostic features of spinel discussed in the text.

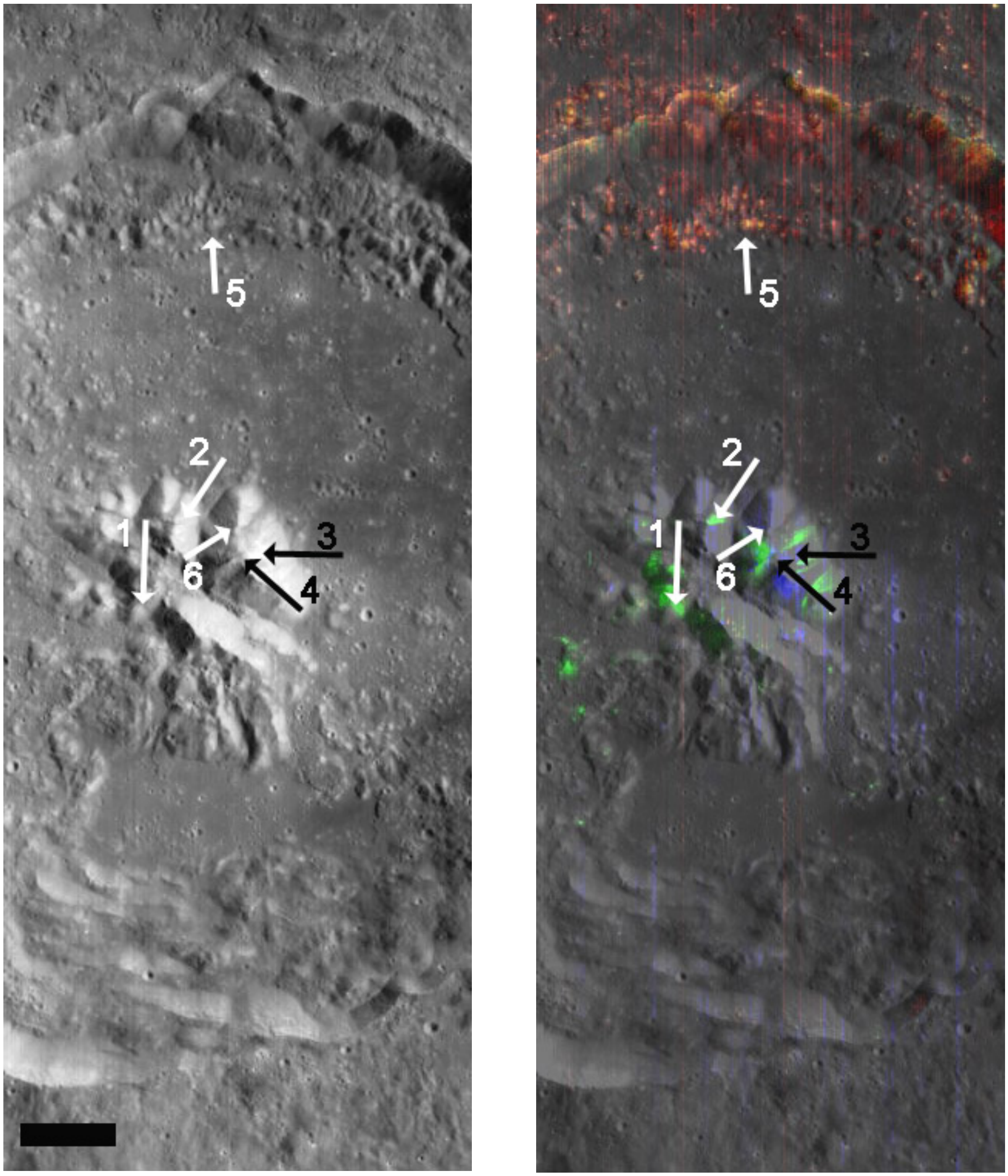

Figure 3. M^3 OP1b images across Theophilus Crater. [Left] M^3 reflectance at 1489 nm retaining local geometry of illumination (*_SUP.IMG PDS data). [Right] Color-composite draped over M^3 reflectance derived from the three M^3 spectral parameters contrast stretched to only indicate the rock type dominated by: Red=pyroxene, Green=spinel, Blue=plagioclase. Arrows indicate location of spectra in Figure 4. Scale bar is 10 km. Spinel is found almost entirely within the peaks; significant pyroxene only occurs in the northern wall. Similar independent data for the later OP2c3 is provided in Figure S3.

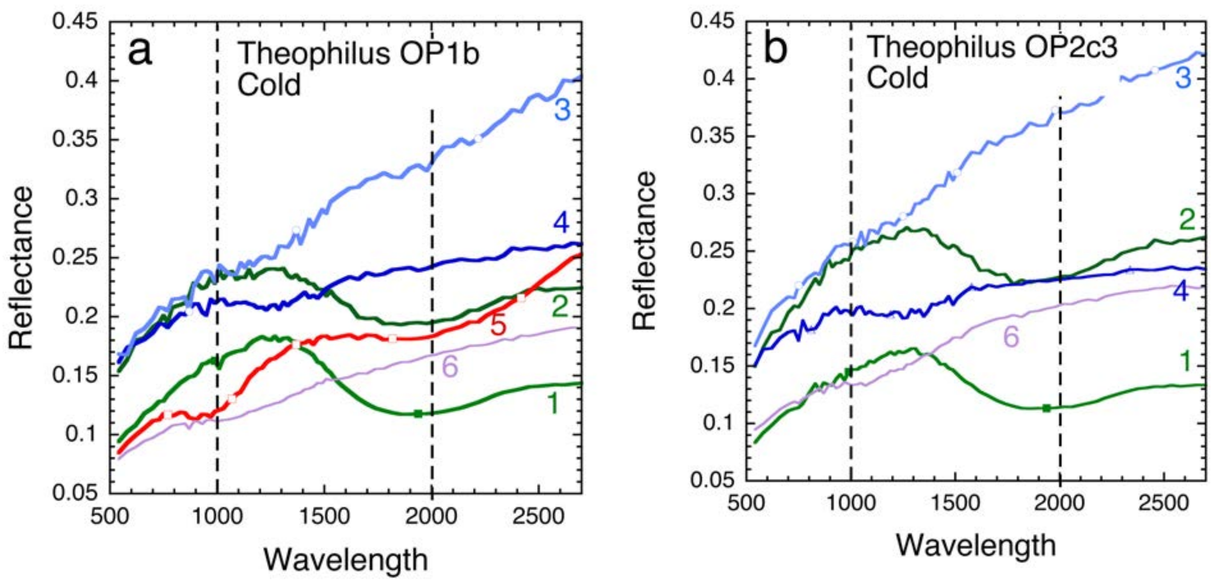

Figure 4. Independent M^3 reflectance spectra obtained for the same areas in Theophilus Crater during two optical periods (OP) that were several months apart. Locations are shown with arrows in Figure 3. All areas except #5 are associated with the central peaks. Additional spectra across the peaks can be found in Figure S4.

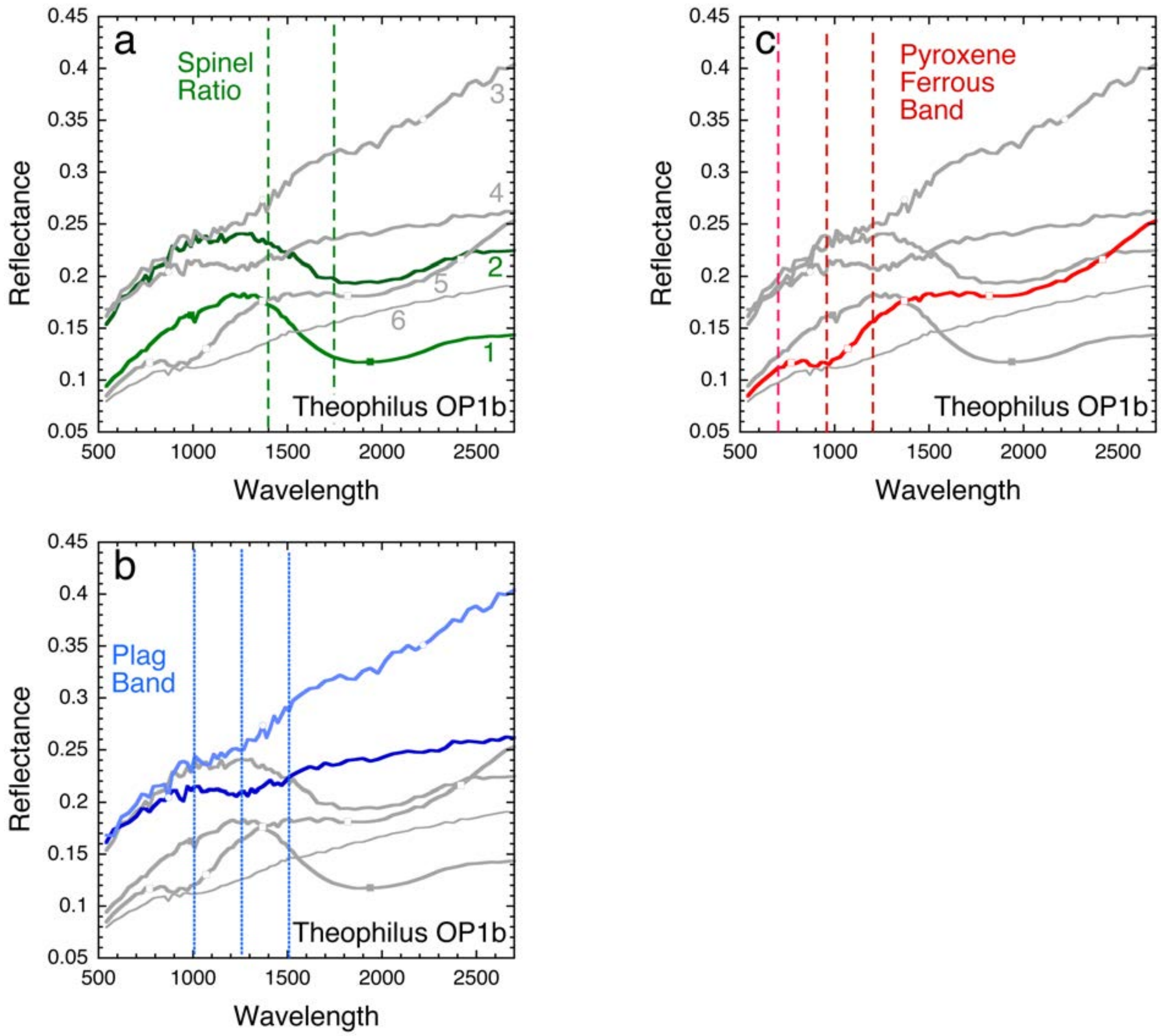

Figure 5. Illustration of spectral parameters used in this analysis to highlight regions in a spatial context that contain prominent features due to specific minerals. Vertical colored lines indicate the wavelengths used for the parameters itemized in Table 1: a) Mg-spinel (green), b) Crystalline plagioclase (blue), c) Pyroxene (red). Example M^3 spectra for areas 1-6 from Fig 4a are used to illustrate features seen in M^3 data.

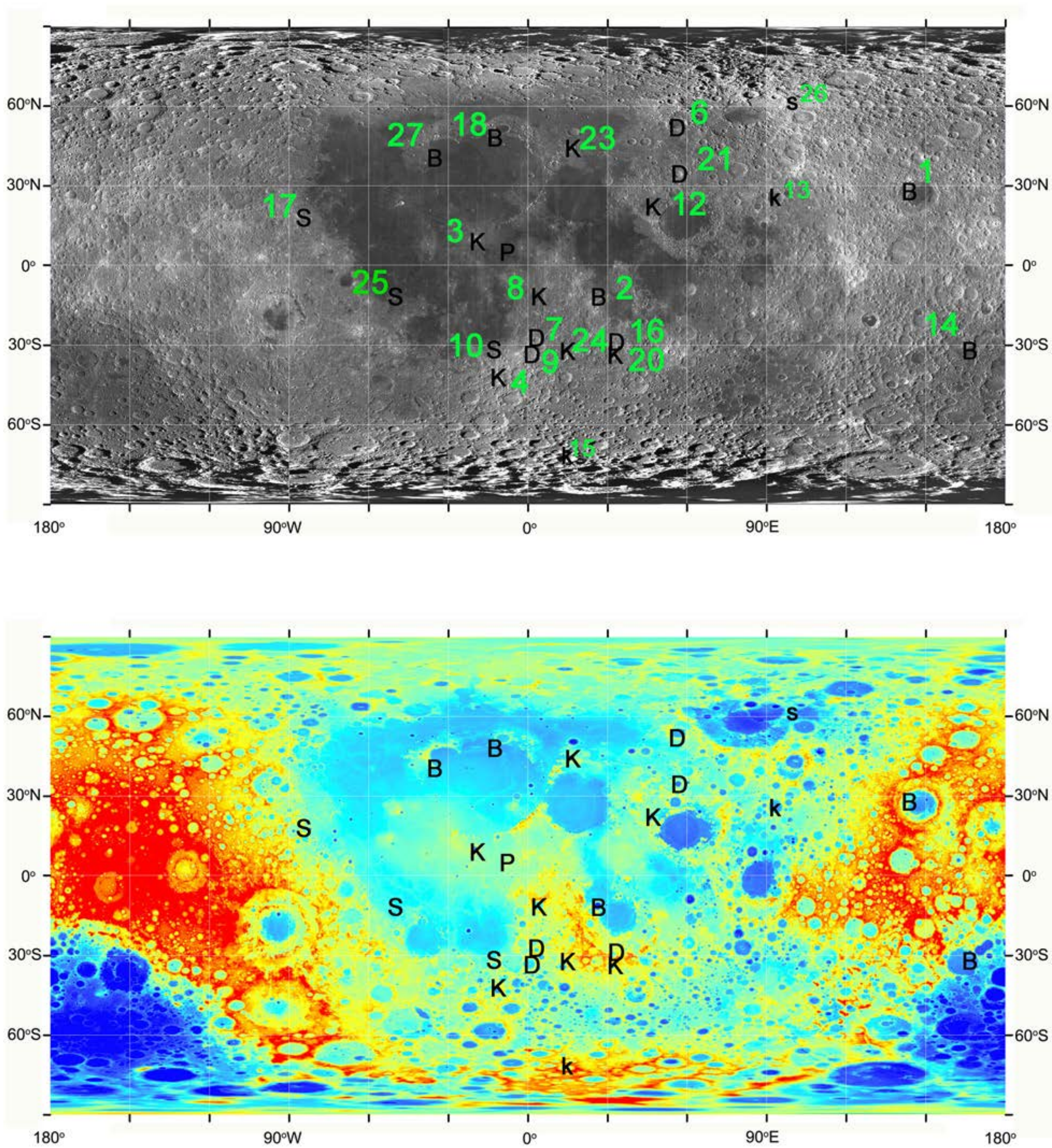

Figure 6 Top, Middle….

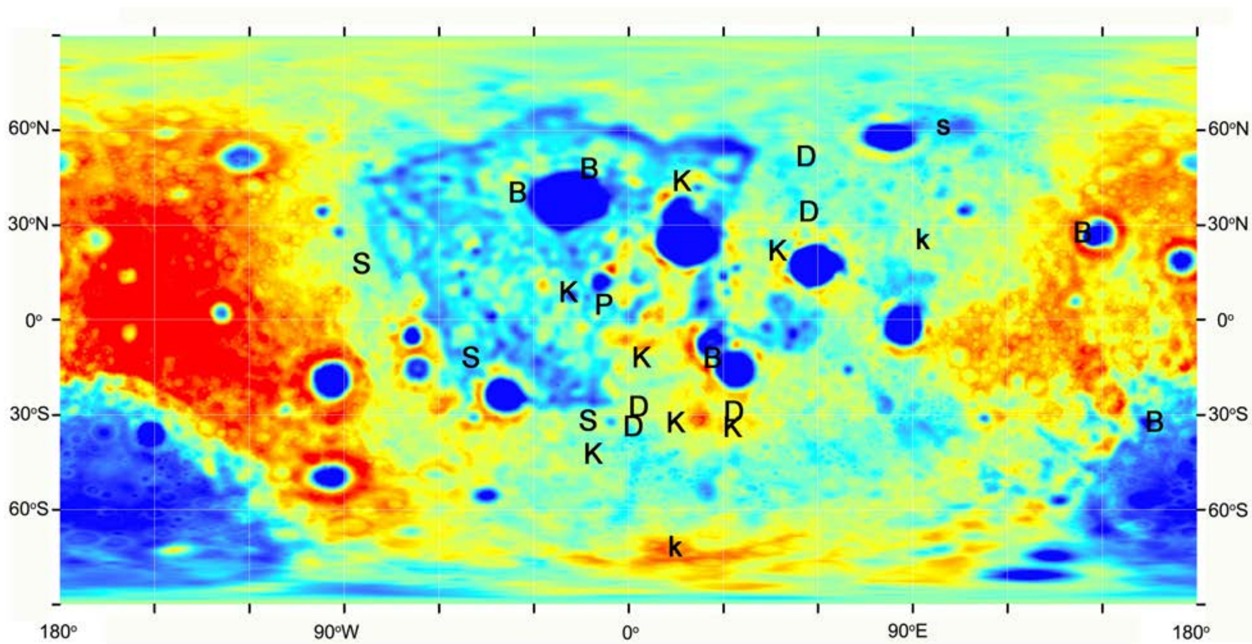

Figure 6. Location of areas with confirmed M^3 identification of spinel. Basemaps are (Top) Lunar Reconnaissance Orbiter Camera (LROC) Wide Angle Camera (WAC) brightness mosaic (Robinson et al. 2010); (Middle) Lunar Orbiter Laser Altimeter (LOLA) topography (Smith et al. 2010); (Bottom) The Gravity Recovery and Interior Laboratory (GRAIL) crustal thickness (Wieczorek et al. 2012). Oversized symbols are centered on the spinel exposure. Categories are discussed in the text. B: Basins; D: dispersed; K: knobs, S: Special; P: pyroclastic. Numbers (in green) are in approximate order of discovery. See Table 2 for specific information on locations.

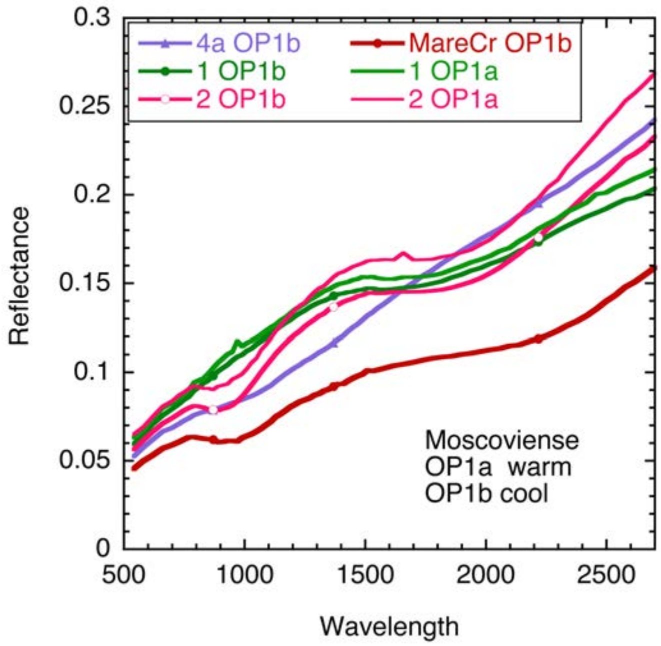

Figure 7. Example M^3 spectra for three of the rock types exposed along the inner ring of Moscoviense basin as measured during two independent optical periods (OP1b and OP1a). Designations for areas 1, 2, 4a are those used in Pieters et al., (2011). Mg-spinel occurs at 1 (green), low-Ca pyroxene at 2 (red), and olivine at 4a (purple). A spectrum from a crater in the mare basalt to the east (MareCr) is provided for comparison (maroon) and exhibits the signature of a more Fe- and Ca-rich clinopyroxene. Color-composite images for Moscoviense similar to Figure 3 for both optical periods can be found in Figure S7.

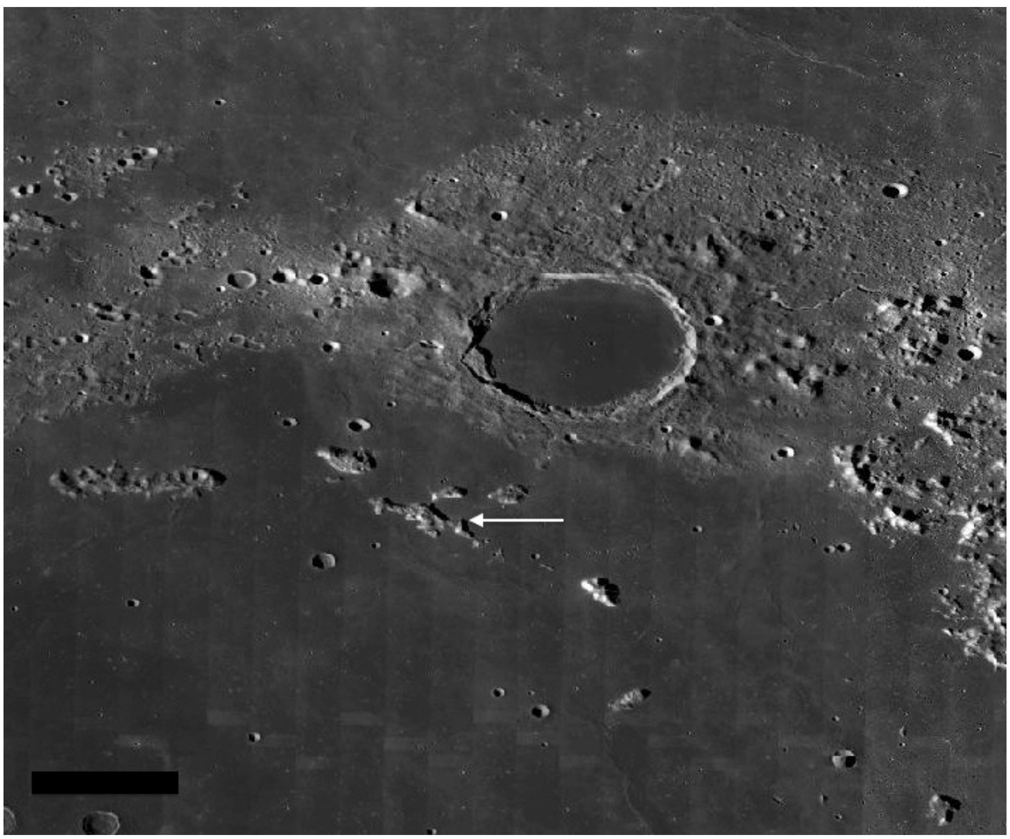

Figure 8. LROC WAC mosaic image of northern Imbrium. Arrow indicates Montes Teneriffe. Scale bar is 100 km.

This is a preprint, the final version is subject to change, of the American Mineralogist (MSA)
Cite as Authors (Year) Title. American Mineralogist, in press.
(DOI will not work until issue is live.) DOI: http://dx.doi.org/10.2138/am-2014-4776

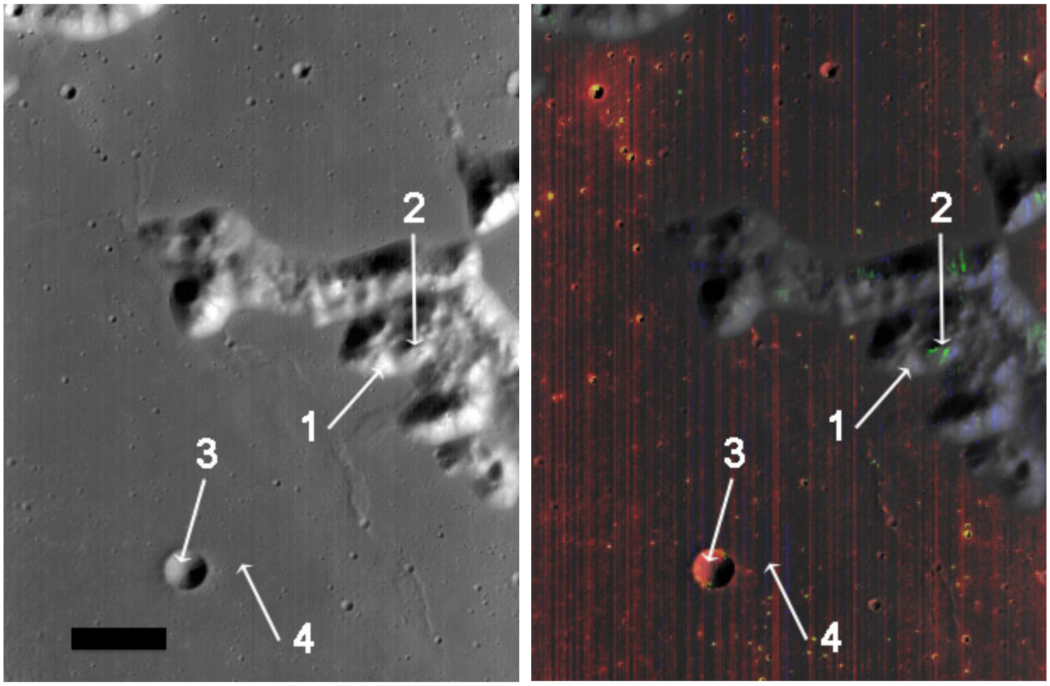

Figure 9. M^3 data for Montes Teneriffe obtained during OP1b. Left: Reflectance image. Right: Rock type color composite (similar to Figure 3). Similar images for independent data acquired with different illumination geometry during OP2a and OP2c1 show the same spatial relations and are provided in Figure S9. Arrows indicate the location of spectra in Figure 10. Scale bar is 10 km.

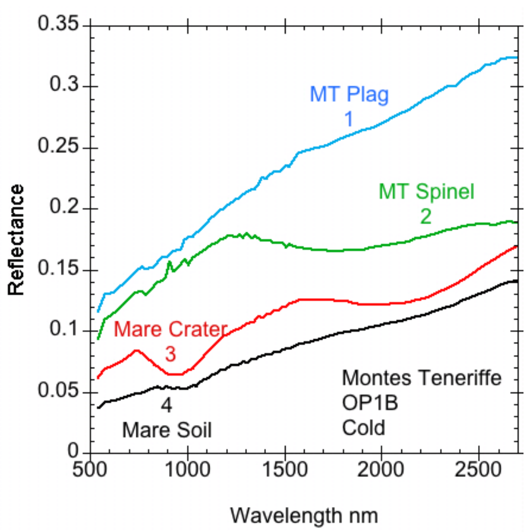

Figure 10. M^3 reflectance spectra for areas in Montes Teneriffe acquired during OP1b. Spectra for the same areas acquired with different illumination geometry during OP2a and OP2c1 are provided in Figure S10 (For OP1b the second spinel area near area 1 was largely in shadow.)

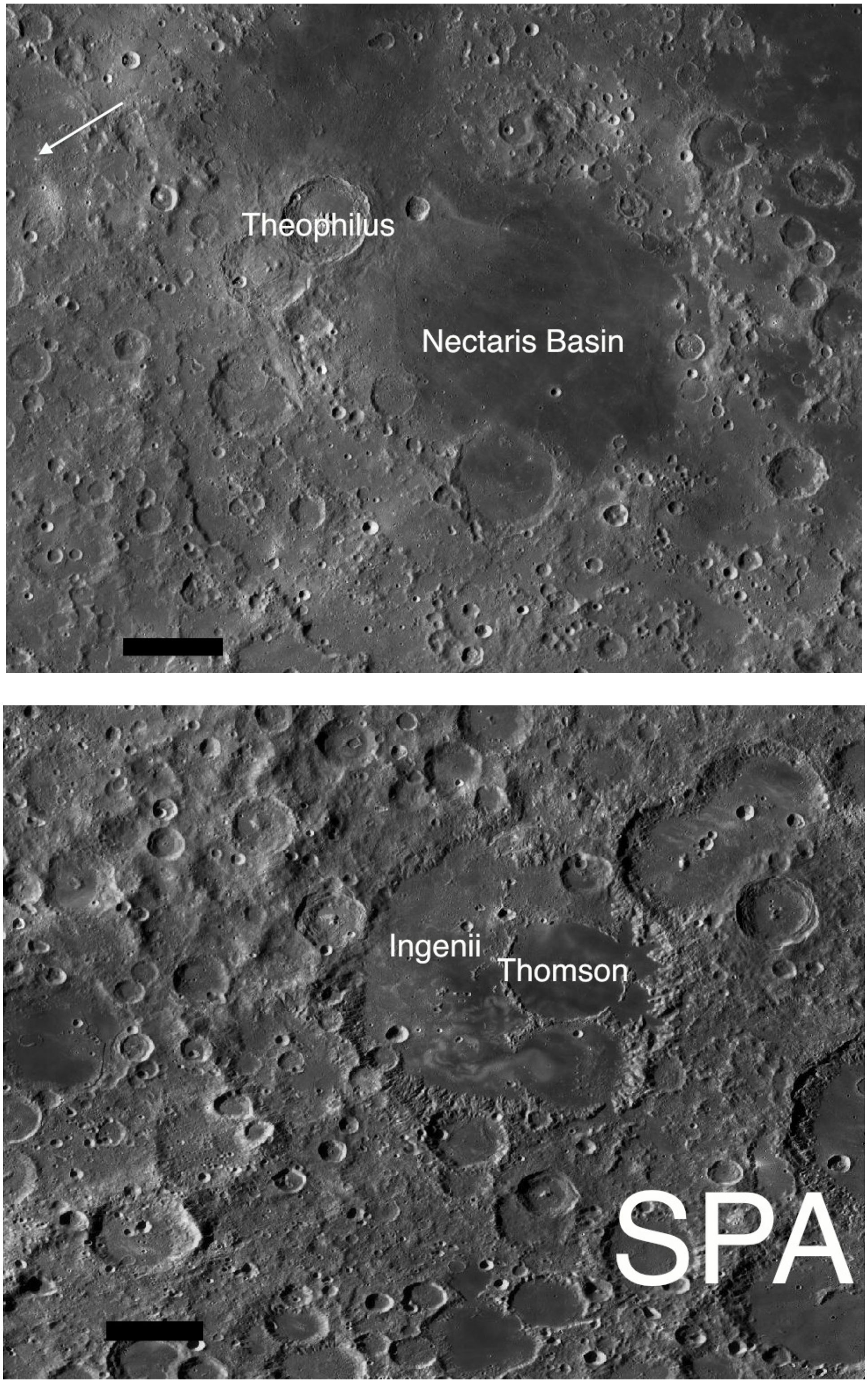

Figure 11. LROC WAC mosaics providing an overview of the Nectaris region containing Theophilus (Top) and the NW portion of South Pole-Aitken basin containing Thomson/Ingenii (Bottom). Scale bar is 100 km. Small white arrow indicates Apollo 16 site.

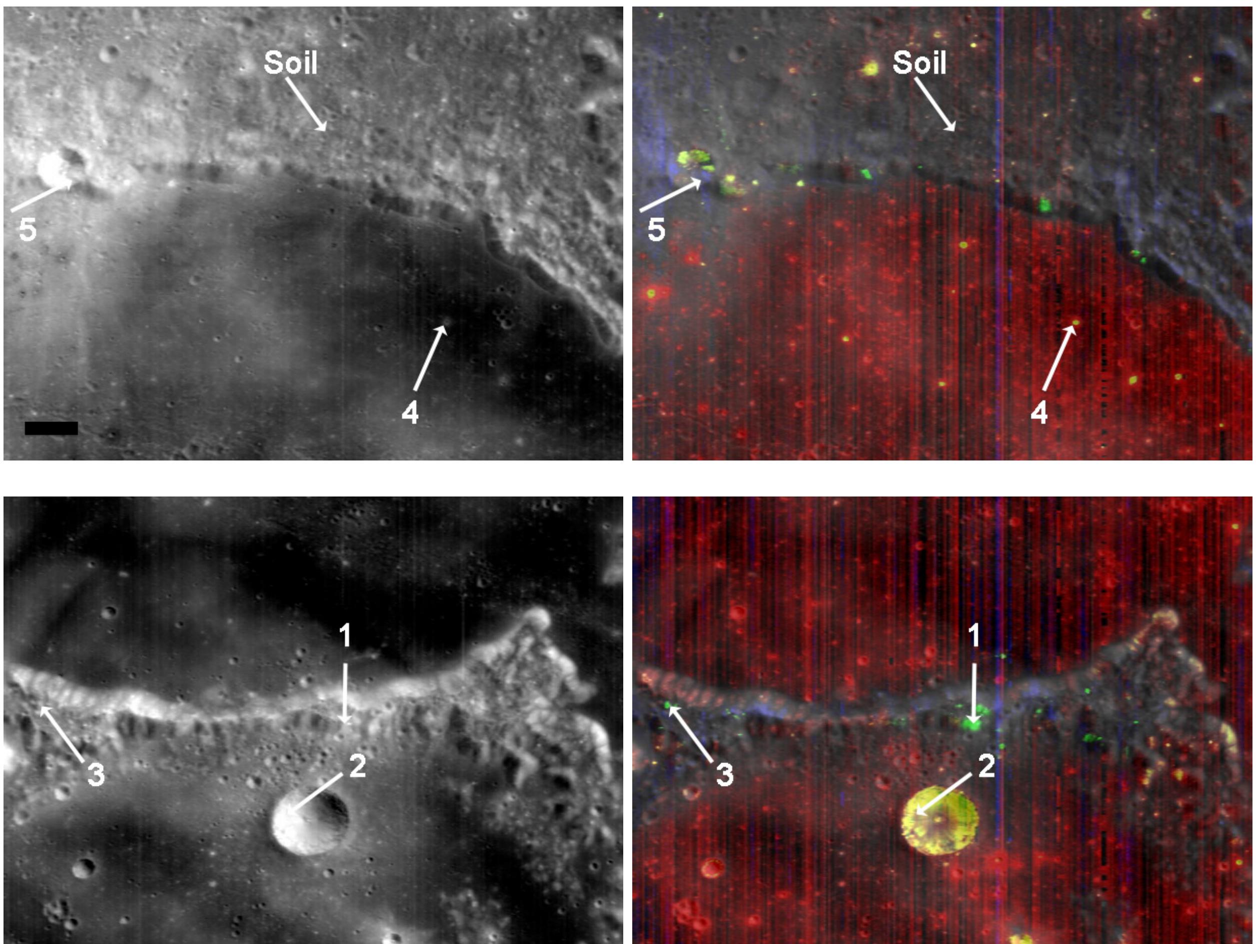

Figure 12. Sub-sections of M^3 data for Thomson acquired during OP2c2 and prepared similar to Figure 3. Top images are the northern rim and bottom images are the southern rim. Left: Reflectance 1489 image (from SUP). Right: rock type color composite superimposed on brightness image. Locations for representative areas 1-5 are indicated with arrows and their spectra are shown in Figure 13. (See Figure S12 for a similar mosaic of independent OP2c1 data across the full Thomson crater.) Scale bar is 10 km.

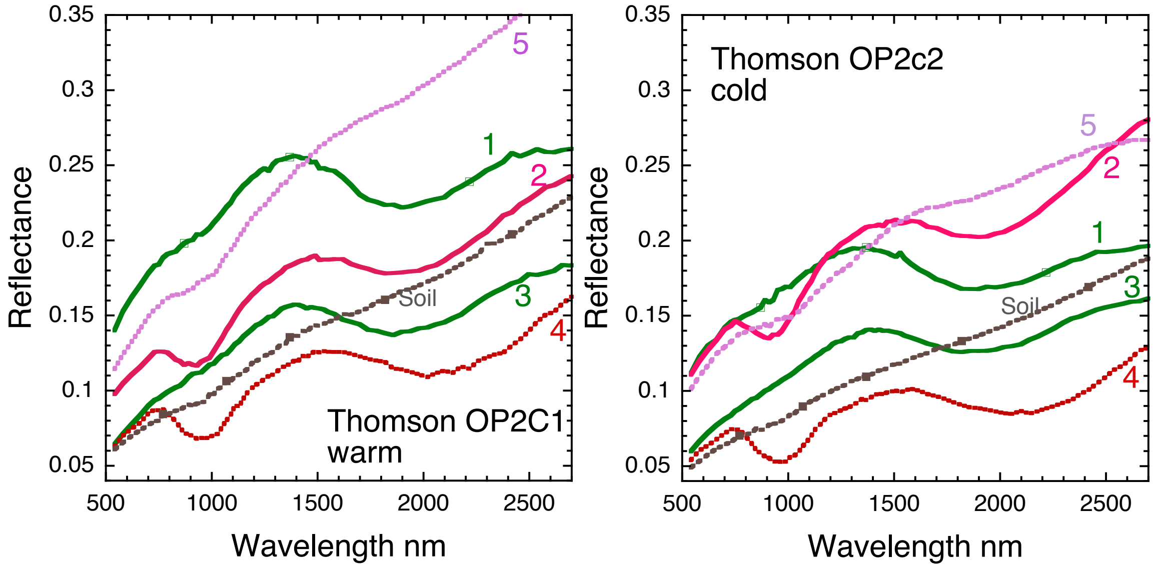

Figure 13. M^3 spectra for the same areas in Thomson acquired during independent periods OP2c1 and OP2c2. Areas along the southern rim are shown in solid lines; areas along the northern rim are in dotted lines. Although the overall spectral properties remain the same between optical periods, differences in brightness for individual areas are due to differences in illumination geometry of the measurements. Spectra for additional Thomson areas from both optical periods are shown in Figure S13.

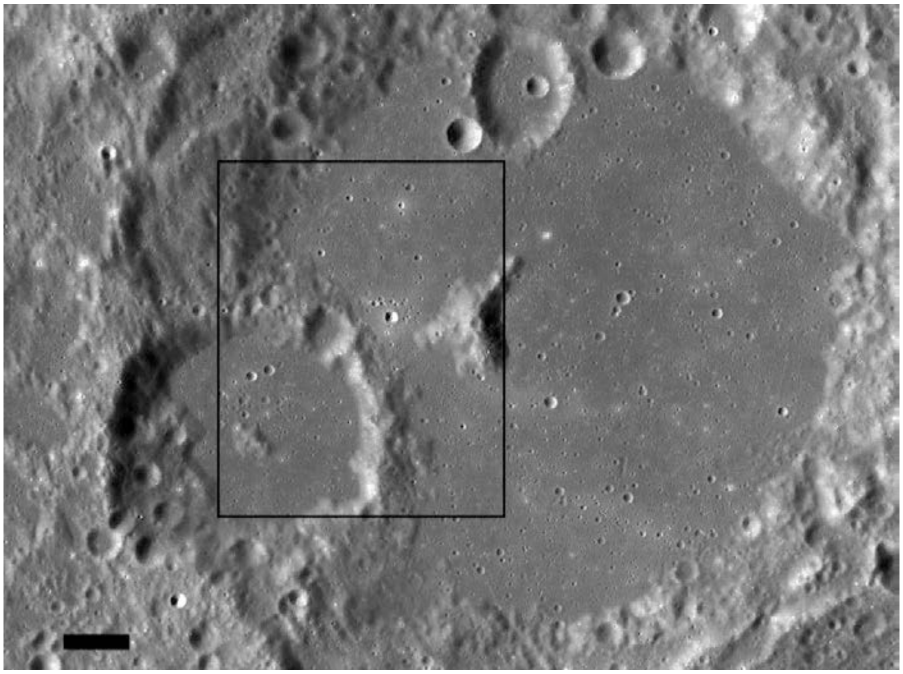

Figure 14. LROC WAC image mosaic of Albategnius (K-8). Scale bar is 10 km. Black box indicates M^3 area in Figure 15.

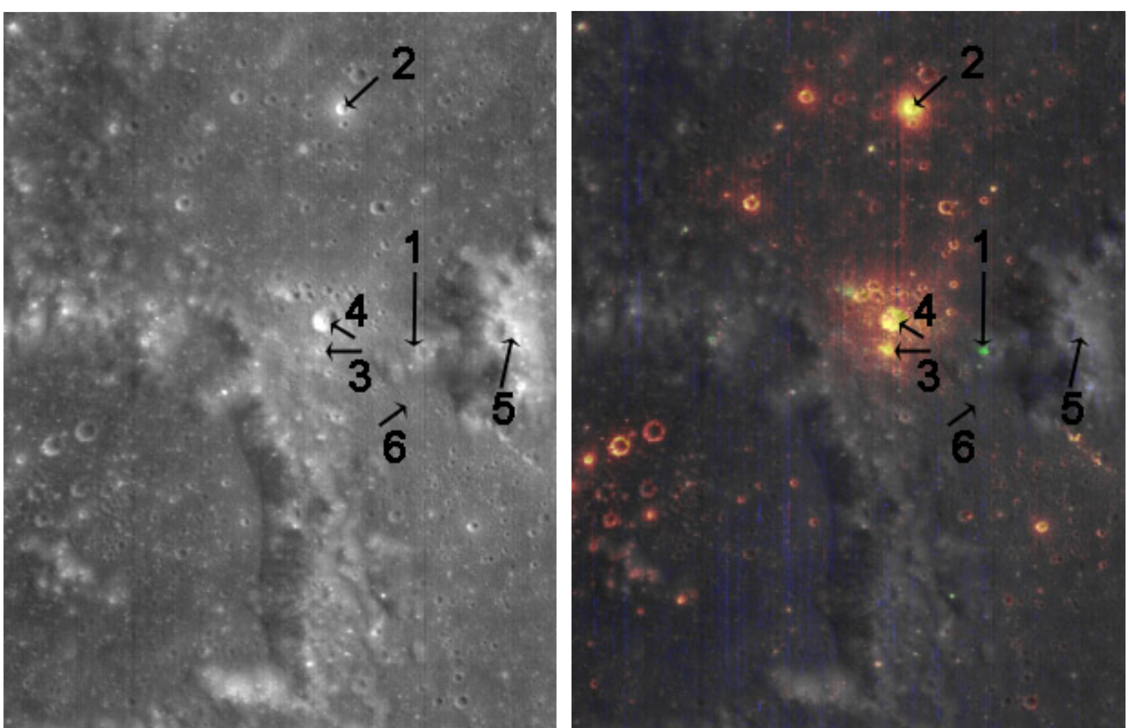

Figure 15. M^3 data for Albategnius (K-8) from OP1a prepared similar to Figure 3. Left: 1489 nm reflectance *SUP image. Right: Rock-type color composite superimposed on brightness image. Arrows indicate locations of areas 1-6

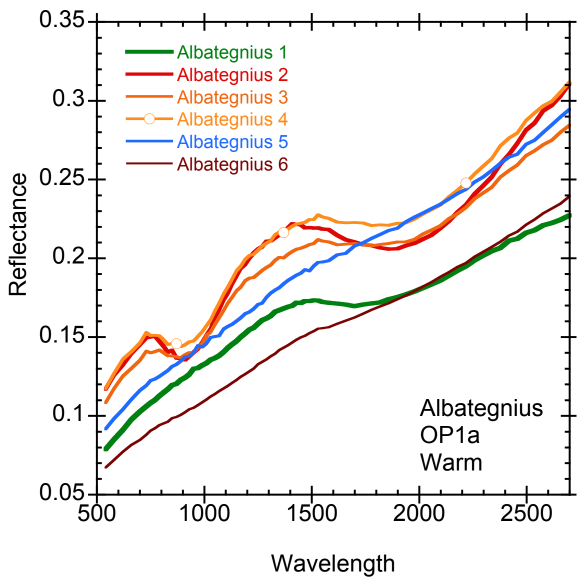

Figure 16. M^3 spectra for the representative areas shown in Figure 15 from OP1a. Independent M^3 spectra for the same areas obtained during optical period OP2c1 are provided in Figure S16 along with reflectance spectra relative to the featureless area Albategnius 5 in order to highlight subtle variations for both optical periods.

This is a preprint, the final version is subject to change, of the American Mineralogist (MSA)
Cite as Authors (Year) Title. American Mineralogist, in press.
(DOI will not work until issue is live.) DOI: http://dx.doi.org/10.2138/am-2014-4776 4/30

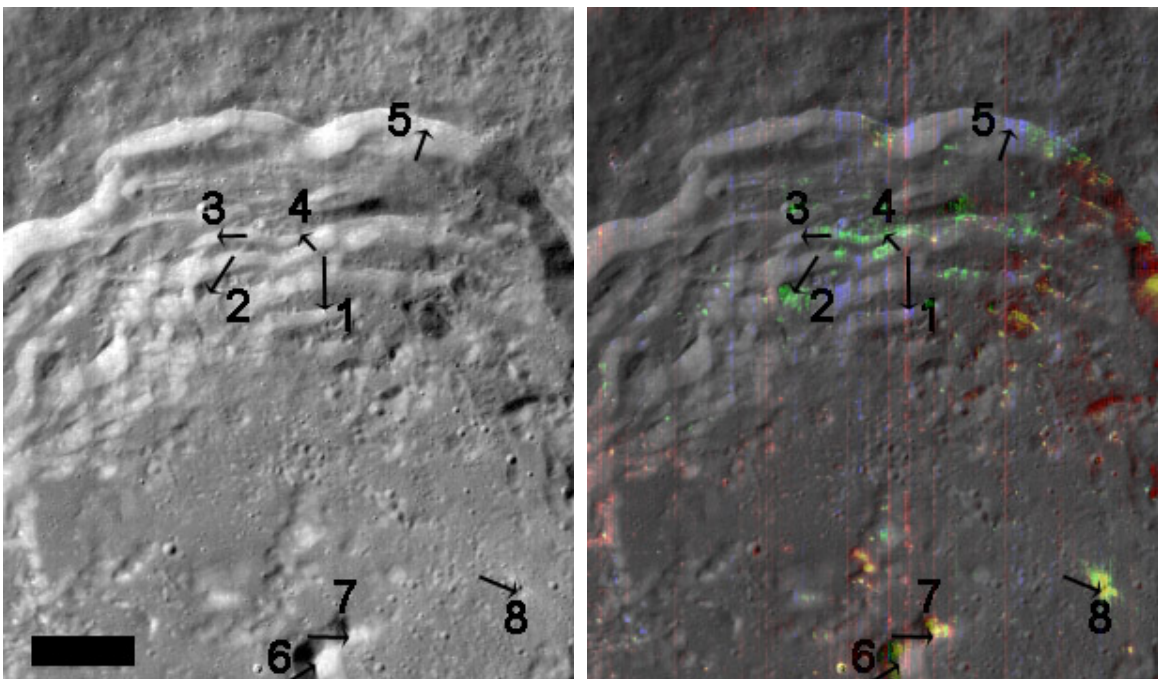

Figure 17. OP1b M^3 data for Geminus (D-21). Left: 1489 nm SUP brightness image. Right: Rock-type color composite (similar to Figure 3 as discussed in the text) superimposed on brightness image. Arrows indicate the location of areas for which spectra were acquired and shown in Figure 18. Scale bar is 10 km.

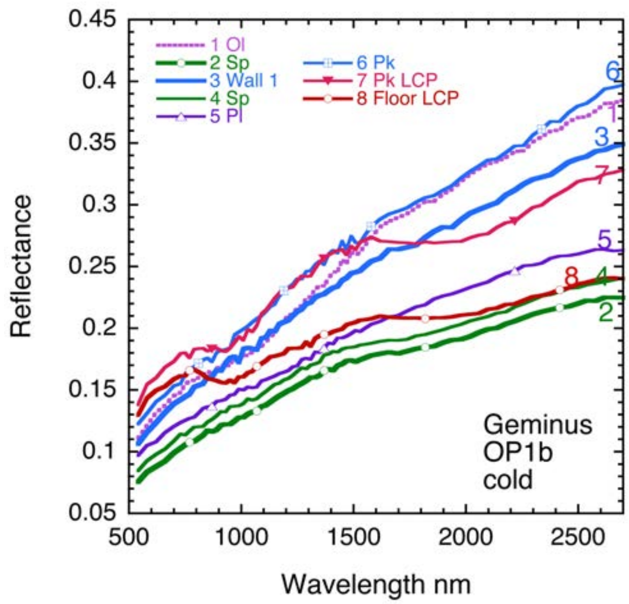

Figure 18. M^3 spectra for representative areas in Geminus shown in Figure 17. Spectra for several of the same areas obtained during independent optical periods OP2c1 and OP2c3 are shown in Figure S18 along with spectra relative to the featureless area Wall 1 in order to allow subtle variations to be highlighted.

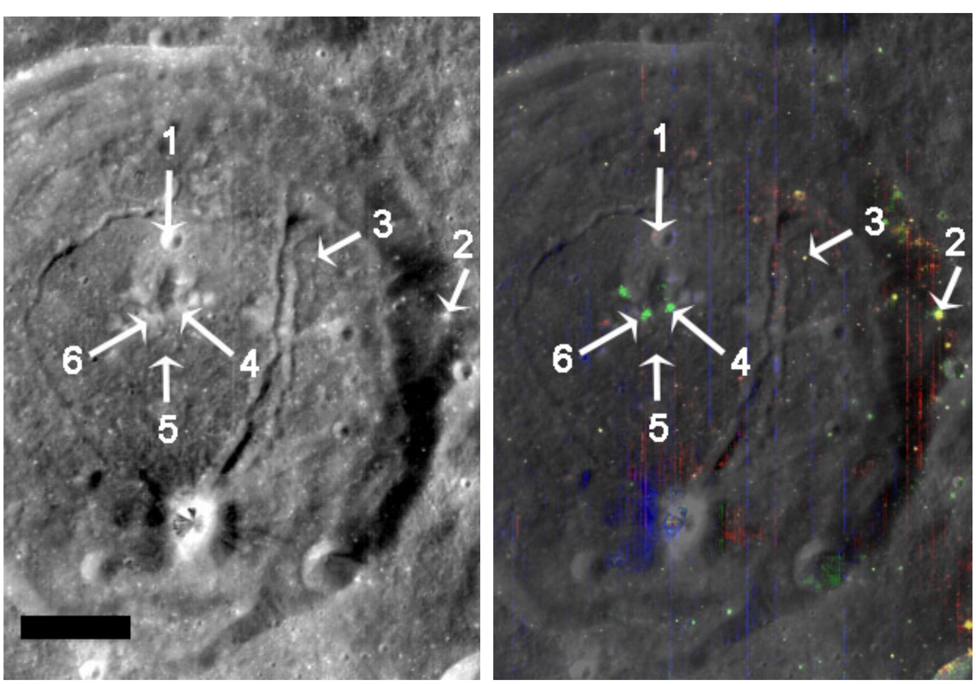

Figure 19. M^3 data for Dalton crater (S-17) from OP1a. Left: 1489 nm *SUP reflectance image. Right: Rock-type color composite similar to Figure 3 superimposed on brightness image. Arrows indicate location for spectra of Figure 20. Scale bar is 10 km. Independent color composites for three additional optical periods are presented in Figure S19.

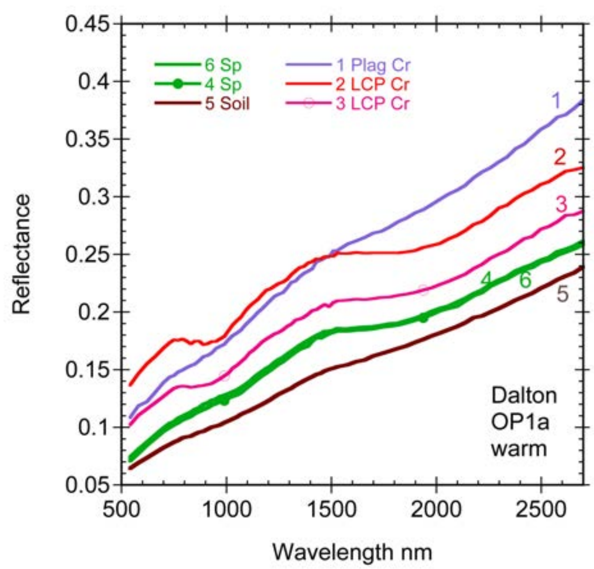

Figure 20. M^3 spectra for areas in Dalton crater shown in Figure 19. Independent Dalton M^3 spectra for the same areas obtained during three additional optical periods with different illumination geometry are shown in Figure S20.

This is a preprint, the final version is subject to change, of the American Mineralogist (MSA)
Cite as Authors (Year) Title. American Mineralogist, in press.
(DOI will not work until issue is live.) DOI: http://dx.doi.org/10.2138/am-2014-4776

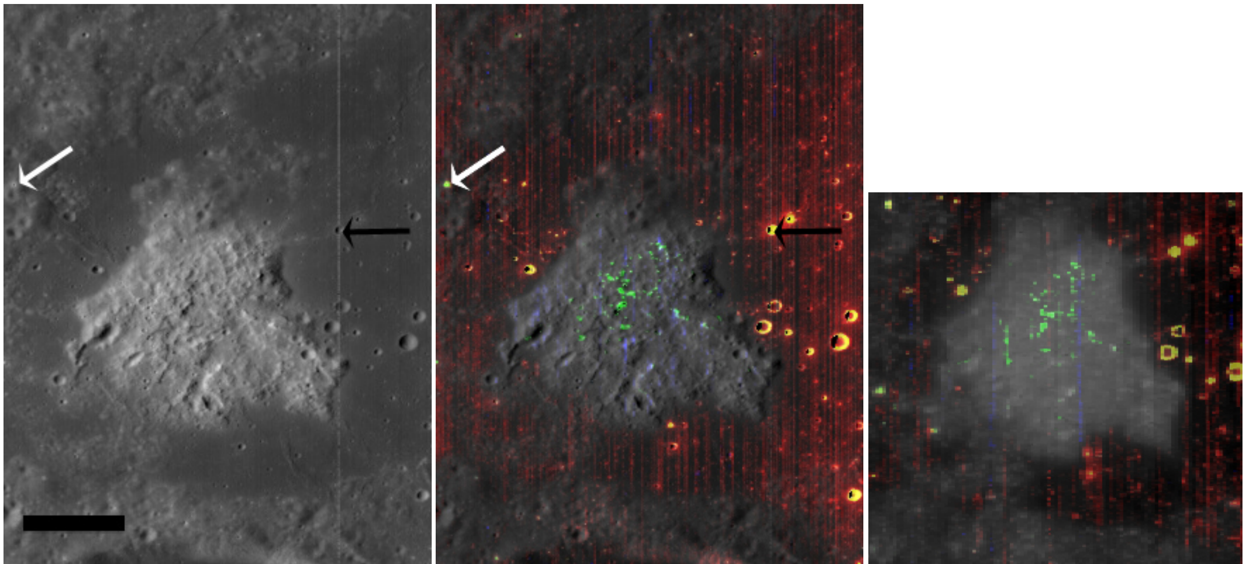

Figure 21. M^3 data for Hansteen Alpha (S-25). Left: 1489 nm *SUP reflectance image from OP2a. Middle: Rock-type color composite similar to Figure 3 superimposed on brightness image for OP2a. Right: Independent rock-type color composite for OP2c1. Scale bar is 10 km.

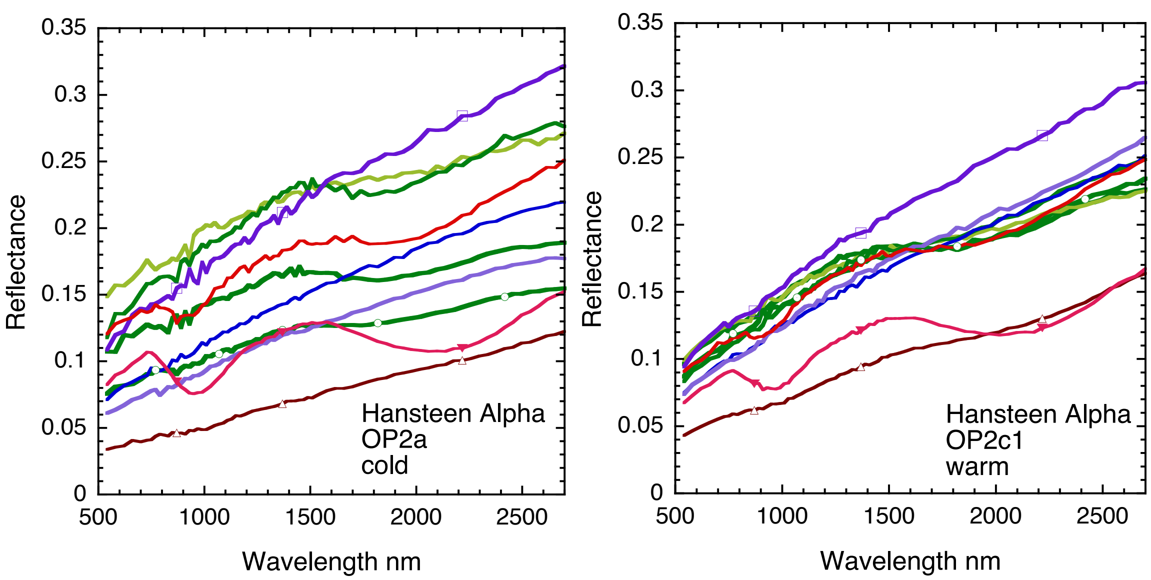

Figure 22. Independent M^3 spectra for the same areas in the Hansteen Alpha region obtained during two different optical periods with different illumination geometry. The green spectra are for four different spinel-bearing areas seen in both optical periods, the blue spectra are for three nearby feldspathic areas. The two pyroxene-bearing areas (red spectra) occur outside Hansteen Alpha and are indicated with a white arrow (low-Ca pyroxene) and a black arrow (high-Ca pyroxene in basalt) on Figure 21. Note that for OP2a the sun was relatively low (illumination angle ~60° from vertical) whereas for OP2c1 the sun was high (illumination angle ~14°). The effect of shadows on variations in measured brightness is thus more prominent for OP2a.

This is a preprint, the final version is subject to change, of the American Mineralogist (MSA)
Cite as Authors (Year) Title. American Mineralogist, in press.
(DOI will not work until issue is live.) DOI: http://dx.doi.org/10.2138/am-2014-4776

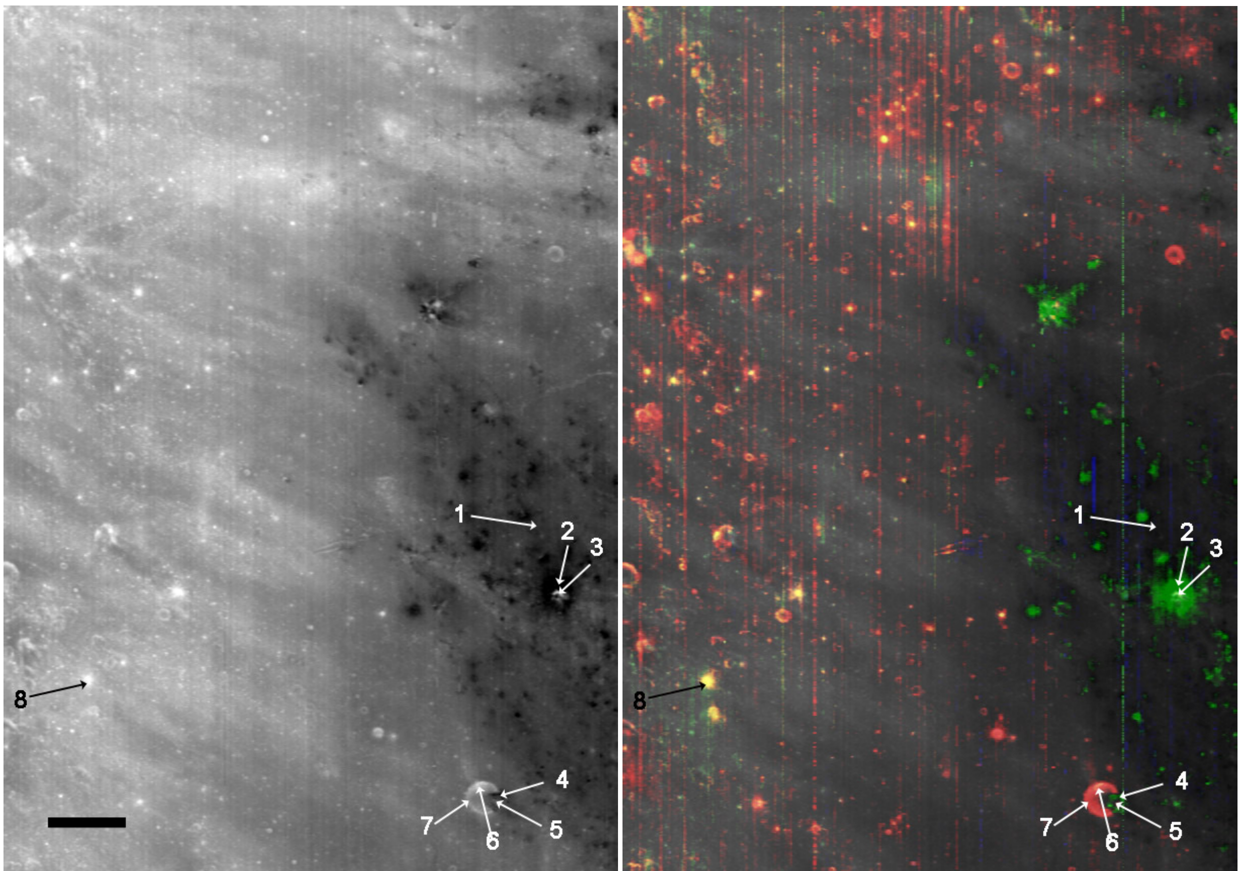

Figure 23. M^3 data covering part of the Sinus Aestuum pyroclastic region obtained during OP2c1 prepared similar to Figure 3. [Left] 700 nm reflectance image. Arrows indicate location of spectra in Figure 24. [Right] Rock-type color composite superimposed on reflectance image. The basaltic terrain to the west of the dark pyroclastic deposits is rich in high-Ca pyroxene. Scale bar is 10 km.

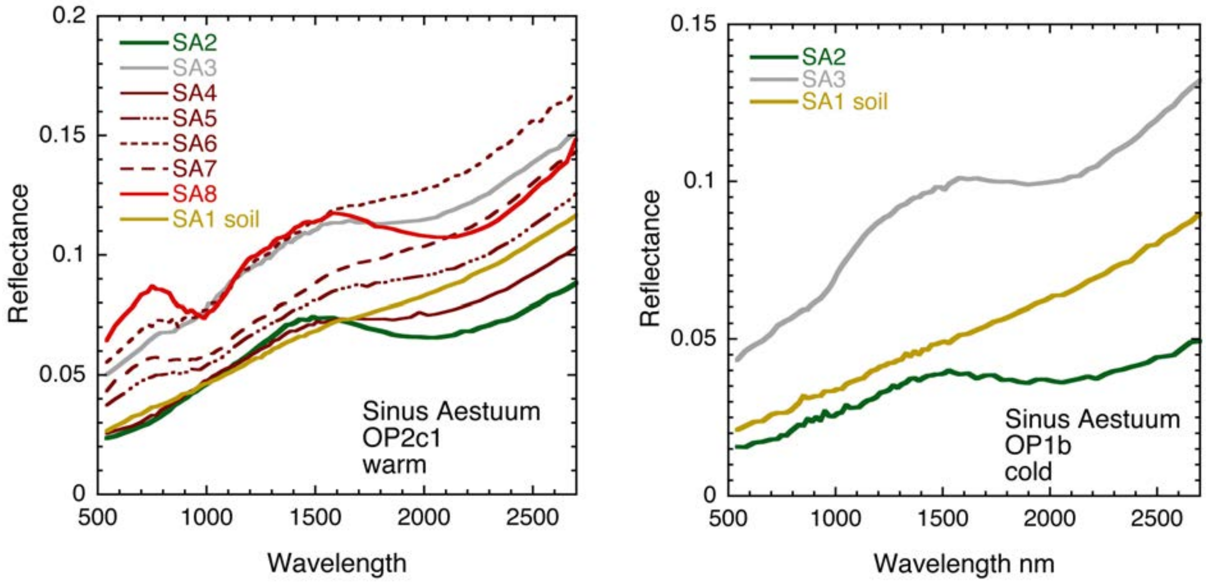

Figure 24. M^3 spectra of the same areas in the Sinus Aestuum region obtained during Optical periods OP2c1 and OP1b. SA1 represents mature soil developed on the pyroclastic deposits. SA2 represents an area of more recently exposed pyroclastic deposit near a crater and SA3 the crater interior. Areas SA4, 5, 6, 7 illustrate mixtures exposed at a ~6 km crater, and SA8 is an example of a normal CPX-rich mare crater.

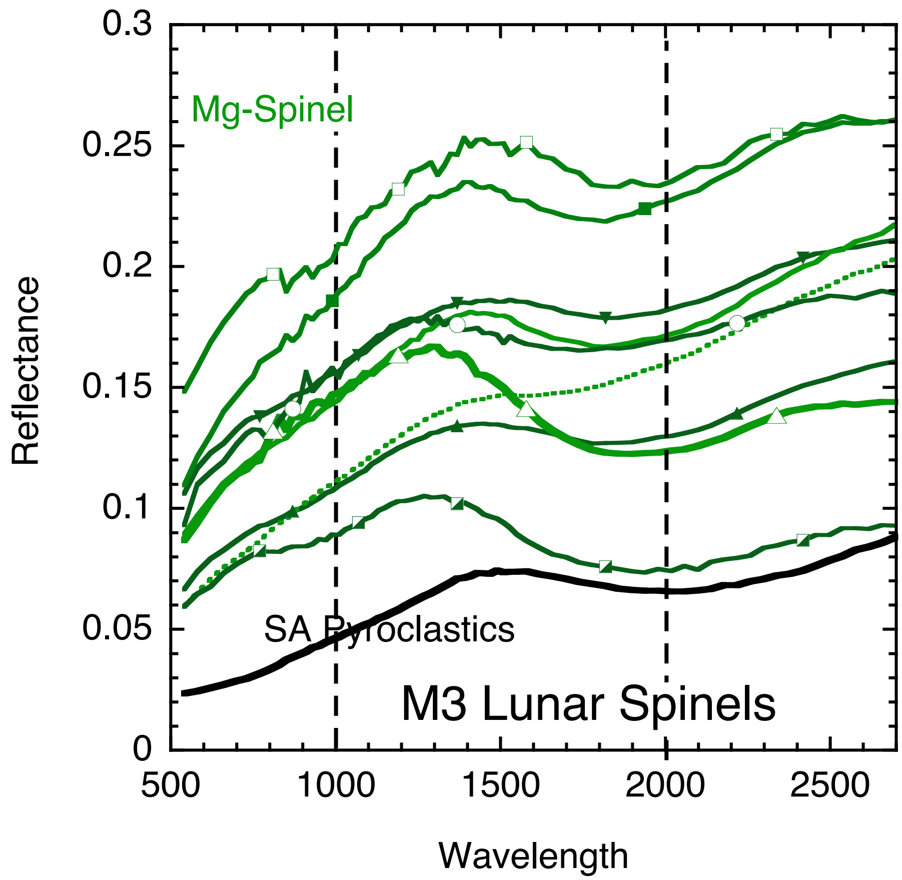

Figure 25. Summary comparison of confirmed M^3 spectra of spinel found in a diversity of geologic settings discussed in the text. Top to bottom at 2100 nm: Endymion1, Endymion2, ThomsonS1, WernerWall1, Montes Teneriffe1, Moscoviense 1, ThomsonS2, TheophilusS1, TychoSp3, Sinus Aestuum2.